

To appear in the Astronomical Journal

HST/WFPC2 and VLA Observations of the Ionized Gas in the Dwarf Starburst Galaxy NGC 4214¹

John W. MacKenty², Jesús Maíz-Apellániz^{2,3}, Christopher E. Pickens⁴, Colin A. Norman^{2,4},
and

Nolan R. Walborn²

ABSTRACT

We present new H α and [O III] λ 5007 narrow band images of the starbursting dwarf galaxy NGC 4214, obtained with the Wide Field and Planetary Camera (WFPC2) onboard the *Hubble Space Telescope* (HST), together with VLA observations of the same galaxy. The HST images resolve features down to physical scales of 2 – 5 pc, revealing several young (< 10 Myr) star forming complexes of various ionized gas morphologies (compact knots, complete or fragmentary shells) and sizes (\sim 10 – 200 pc). Our results are consistent with a uniform set of evolutionary trends: The youngest, smaller, filled regions that presumably are those just emerging from dense star forming clouds, tend to be of high excitation and are highly obscured. Evolved, larger shell-like regions have lower excitation and are less extincted due of the action of stellar winds and supernovae. In at least one case we find evidence for induced star formation which has led to a two-stage starburst. Age estimates based on $W(\text{H}\alpha)$ measurements do not agree with those inferred from wind-driven shell models of expanding H II regions. The most likely explanation for this effect is the existence of an \approx 2 Myr delay in the formation of superbubbles caused by the pressure exerted by the high density medium in which massive stars are born. We report the detection of a supernova remnant embedded in one of the two large H II complexes of NGC 4214. The dust in NGC 4214 is not located in a foreground screen but is physically associated with the warm ionized gas.

¹Based on observations with the NASA/ESA *Hubble Space Telescope* and the NRAO *Very Large Array*. The HST observations were obtained at the Space Telescope Science Institute, which is operated by the Association of Universities for Research in Astronomy, Inc. under NASA contract No. NAS5-26555. The National Radio Astronomy Observatory is a facility of the National Science Foundation operated under cooperative agreement by Associated Universities, Inc.

²Space Telescope Science Institute, 3700 San Martin Drive, Baltimore, MD 21218, U.S.A.

³Laboratorio de Astrofísica Espacial y Física Fundamental-INTA, Apdo. Postal 50727, E-28080 Madrid, Spain.

⁴Henry A. Rowland Department of Physics and Astronomy, The Johns Hopkins University, Baltimore, Maryland 21218, U.S.A.

Subject headings: dust, extinction — galaxies: individual (NGC 4214) — galaxies: irregular — ISM: evolution — supernova remnants

1. INTRODUCTION

NGC 4214 is an emission-line selected dwarf galaxy. It was chosen for observation based on a study of a complete sample of galaxies from the Center for Astrophysics redshift survey (CfARS; Huchra et al. 1983) presented by Burg (1987)⁵. The Burg study, which included emission line data for the galaxy, noted that NGC 4214 possesses optical emission line ratios ($\log [\text{O III}] \lambda 5007 / \text{H}\beta > 0.2$ and $\log [\text{N II}] \lambda 6584 / \text{H}\alpha < -0.6$) that are similar to those of giant H II regions and other starbursts (Baldwin et al. 1981). Its metallicity has been measured by Kobulnicky & Skillman (1996), who find $12 + \log(\text{O/H}) = 8.20 - 8.36$. The distinguishing qualities of this object are: (1) It is among a set of the most highly excited photoionized galaxies of the CfARS. (2) It is listed as a Wolf-Rayet galaxy (Schaerer et al. 1999), exhibiting broad He II 4686 Å emission in the heart of its brightest clusters (Sargent & Filippenko 1991; Mas-Hesse & Kunth 1991). (3) It is very bright at UV continuum wavelengths (Fanelli et al. 1997). NGC 4214 has a $M_B^0 \approx -18.8$ if located at a distance of 4.1 Mpc (Leitherer et al. 1996), the value which will be used in this article, even though Hopp et al. (2000) suggest that it could be somewhat closer.

The brightness of NGC 4214 in the UV may be related to its apparently low dust content. The dust mass, inferred from its far-IR continuum luminosity, L_{IR} ($\sim 1.1 \cdot 10^9 L_\odot$, Thronson et al. 1988), is $1.8 \cdot 10^5 M_\odot$, much smaller than dust masses typically found in Ultraluminous Infrared Galaxies and even among other dwarf starbursts. Furthermore, the ratio $\log(L_{\text{IR}}/L_{\text{UV}})$ is ~ 0.82 , much smaller than is found for most of the UV bright starbursts observed with IUE (Heckman et al. 1998). This indicates that most of the observed UV emission is not reprocessed into far-IR emission via dust absorption on global scales. Geometry may play a large role, since NGC 4214 has a nearly face on orientation on the sky (Allsopp 1979) and apparently a thin disk (Maíz-Apellániz et al. 1999, hereafter, MMTM). However, there are subgalactic variations of dust extinction which complicate our analysis. Maíz-Apellániz et al. (1998) (hereafter, MMMVC) report irregular variations of $E(B - V)$ on scales of order $\sim 0.1\text{--}0.6$ arcseconds, based on their spatial map of Balmer line ratios in the inner regions of the galaxy.

⁵The CfARS consisted of 2400 galaxies taken from the original Zwicky Catalog to a limiting magnitude of $M_B^0 = 14.5$.

2. OBSERVATIONS AND DATA REDUCTION

2.1. HST/WFPC2 imaging

We obtained deep, high resolution, multiwavelength imaging of NGC 4214 with the WFPC2 instrument aboard HST (prop. ID 6569) on 1997 July 22. In Figure 1 we show a graphic representation of the WFPC2 field superimposed on a $13'.6 \times 13'.6$ greyscale reproduction of the Digitized Sky Survey Image⁶. The equatorial coordinates of the intersection point of the four camera fields are $\alpha = 12^{\text{h}}15^{\text{m}}40\text{:}53$, $\delta = 36^{\circ}19'37\text{''}$ (J2000). This location was chosen in order to minimize Charge Transfer Efficiency (CTE) effects, since in this way no area of interest is separated from its collecting point by low signal areas (Whitmore et al. 1999). At a distance of 4.1 Mpc, $1'' = 20$ pc, so that one WF pixel corresponds to 2.0 pc and one PC pixel to 0.91 pc. Spatial resolution on these physical scales is within a factor of 2 – 4 of the best resolution that can be achieved from the ground for the LMC. Thus, the high spatial resolution, high sensitivity, wide dynamical range and faint magnitude limit (roughly 3 magnitudes fainter than typical ground-based limits, ~ 26 in V) of WFPC2 permits one to identify regions structurally similar to those in the LMC (e.g. 30 Doradus), with ground-based resolution quality, for objects at nearly 80 times the distance to the LMC. Throughout the remainder of this paper, all conversions between pixels and arcseconds/physical scales are based on the plate scale of the WF chips, where most of NGC 4214 was imaged.

We summarize the WFPC2 data set analyzed for this study in Table 1. A set of 15 HST/WFPC2 exposures was collected with 2 narrow band and 4 continuum filters. The continuum exposures consisted of two long ones and a short one. The short exposure was obtained in order to correct for the possible saturation at the location of strong point sources (unfortunately, the short F702W exposure was lost). The gain on the WF chips was $7e^- DN^{-1}$. Due to the limited observing time and the desire to carefully remove cosmic ray events, we did not apply dithering techniques during the observing period, commonly used to partially compensate for the undersampled nature of the Point Spread Function (PSF).

The entire HST/WFPC2 data set was processed using the STScI WFPC2 pipeline. The images were then reduced and analyzed using various standard IRAF⁷ packages as well as IDL procedures developed specially for this purpose. Detailed photometric analysis of the continuum images will be presented in a later discussion (Paper II), which will compare some of the results of the resolved

⁶Based on photographic data of the National Geographic Society – Palomar Observatory Sky Survey (NGS-POSS) obtained using the Oschin Telescope on Palomar Mountain. The NGS-POSS was funded by a grant from the National Geographic Society to the California Institute of Technology. The plates were processed into the present compressed digital form with their permission. The Digitized Sky Survey was produced at the Space Telescope Science Institute under US Government grant NAG W-2166.

⁷IRAF (Image Reduction and Analysis Facility) is distributed by the National Optical Astronomy Observatories, which are operated by AURA, Inc., under cooperative agreement with the National Science Foundation.

stellar populations of NGC 4214 with the integrated line emission measurements made in this study. Here we will use the continuum images only for continuum subtraction of the narrow band images and for integrated photometry at the wavelength of $\text{H}\alpha$.

We used our multiple exposures to account for cosmic rays and we eliminated hot pixels and other defects. Each chip was flux calibrated using the corresponding PHOTFLAM keywords, the sky (or zero point offset) was subtracted, and we finally coadded the images to produce deep mosaics.

The analysis of the mosaics revealed that all the F702W, F555W, and F336W exposures were saturated at the location of knot I-As (the knot nomenclature is explained in the next section). Also, the two F702W exposures were saturated at knot IIIIs (the nucleus of the galaxy). To eliminate the effect in the F555W and F336W exposures, we used archival WFPC2 images from proposal 6716 (P.I.: T. P. Stecher) in which knot I-As was detected in the PC chip instead of in the WF3 one. The smaller pixel size allowed knot I-As not to be saturated in the F336W filter and to suffer only from slight saturation in the F555W, which was easily corrected. We used those images to substitute the saturated pixels and their neighbors. Unfortunately, no F702W images were available to correct for the saturation at knots I-As and IIIIs. Therefore, in that case we could only substitute the affected pixels by a linear combination of the F555W and F814W images, a procedure that introduces a small uncertainty in the $\text{H}\alpha$ continuum for those knots, the relevant quantity which will be used in this paper (see below).

To eliminate the contribution of the continuum to the narrow band images and that of line emission to the continuum F555W and F702W images, we developed the following procedure. First, we assumed that the only nebular lines contributing to the continuum images were $\text{H}\alpha$, $[\text{O III}] \lambda 4959 + 5007$, and $\text{H}\beta$, with fixed ratios $[\text{O III}] \lambda 5007 / [\text{O III}] \lambda 4959 = \text{H}\alpha / \text{H}\beta = 3.0$, and we neglected other lines such as $[\text{N II}] \lambda 6548 + 6584$ and $[\text{S II}] \lambda 6717 + 6731$. Second, we approximated the spectral continuum flux at 5007 Å, $F(\lambda 5007)$, as the average spectral continuum flux for the F555W filter, $F(V)$, and the one at $\text{H}\alpha$, $F(\lambda 6563)$, by a linear combination of $F(V)$ and $F(R)$ (the average spectral continuum flux for the F702W filter), with coefficients determined from the STSDAS package SYNPHOT. Finally, we used SYNPHOT again to produce the following linear system:

$$\begin{aligned}
 F(702W) &= 1.00 F(R) &+& 0.99 F(\text{H}\alpha)/w_1 \\
 F(656N) &= 0.76 F(R) + 0.24 F(V) &+& 1.00 F(\text{H}\alpha)/w_2 \\
 F(555W) &= & 1.00 F(V) &+ 0.36 F(\text{H}\alpha)/w_3 &+& 1.00 F([\text{O III}] \lambda 5007)/w_3 \\
 F(502N) &= & 1.00 F(V) & &+& 1.00 F([\text{O III}] \lambda 5007)/w_4
 \end{aligned} \tag{1}$$

Here, $F(702W)$, $F(656N)$, $F(555W)$, and $F(502N)$ are the PHOTFLAM calibrated measured spec-

tral fluxes⁸, $F(\text{H}\alpha)$ and $F(\text{[O III]} \lambda 5007)$ are the true line fluxes and $w_1 \dots w_4$ are the effective widths of each filter (in Angstroms). We solved the linear system and dropped the smaller terms to obtain:

$$\begin{aligned}
 F(\text{R}) &= 1.014 F(702\text{W}) - 0.018 F(656\text{N}) \\
 F(\text{V}) &= 1.027 F(555\text{W}) - 0.025 F(502\text{N}) - 0.006 F(656\text{N}) \\
 F(\text{H}\alpha) &= 29.9 (1.017 F(656\text{N}) - 0.773 F(702\text{W}) - 0.250 F(555\text{W})) \\
 F(\text{[O III]} \lambda 5007) &= 35.6 (1.027 F(502\text{N}) - 1.025 F(555\text{W}))
 \end{aligned} \tag{2}$$

As is always the case when two measured quantities are subtracted, the final relative uncertainty is largest for the case when the result is much less than the terms which are being subtracted. That would be the situation when we want to calculate line fluxes where only stars are present or continuum fluxes where there is mostly gas. The first case may apply to some small apertures around isolated star clusters. However, given that most of the star forming episodes in NGC 4214 are quite recent (with large values of $W(\text{H}\alpha)$ and $W(\text{[O III]} \lambda 5007)$), the corrections for the line fluxes (and the corresponding increase in the relative uncertainties) will always be small for large apertures and the largest uncertainty will always be the absolute photometric calibration of the narrow band filters. The second case becomes important when the equivalent width of the line is comparable to the effective width of the filter, which occurs only in some very extreme situations for $\text{H}\alpha$ or $\text{[O III]} \lambda 5007$ (as will be shown later). Even then, since the estimated uncertainty in the coefficients which appear in the subtracting terms in Eq. 2 is not larger than 15%, the final uncertainty will also be smaller than that. That number should be compared with the error that occurs if no correction is applied at all: since up to 50% of the flux registered with the F555W or F814W filters may be actually coming from emission line photons, we may overestimate the continuum flux by a factor of two.

2.2. VLA observations

NGC 4214 was observed with the NRAO Very Large Array (VLA) on 1988 April 24 in the C configuration at 6 cm (4.885 GHz) and on 1989 March 16 in the B configuration at 20 cm (1.465 GHz). These wavelength - configuration combinations each result in synthesized beam diameters of approximately 4 arcseconds. On-target integration times were 855 seconds at 6 cm and 700 seconds at 20 cm. The integrations each were divided into two segments so that a larger range in hour angle (and a better sampling of the UV plane) might be achieved.

The observations were edited to exclude bad antennas and samples. 3C286 was used as a primary flux calibrator for both observations and phase calibrators were selected from the VLA

⁸Note that the standard WFPC2 flux calibration produces spectral fluxes even for narrow band filters.

recommended sample. The data were converted to maps using the standard AIPS software in 1989/90 with a 1 arcsecond pixel size. The MX task was used to map and CLEAN the uv data. The resulting maps have rms noise levels of approximately 0.08 mJy at 6 cm and 0.13 mJy at 20 cm.

3. THE STRUCTURES OF THE IONIZED GAS

3.1. Narrow band morphology

3.1.1. Global structure

We show in Figs. 2 and 3 the two WFPC2 narrow band images ($\text{H}\alpha$ and $[\text{O III}] \lambda 5007$) on a logarithmic scale after continuum subtraction. We also show in Fig. 4 the $\text{H}\alpha$ continuum ($\lambda 6563$) image produced as described in the previous section. The three images are combined into a three color mosaic in Fig. 5.

The narrow band morphology shows three differentiated components in NGC 4214:

1. Two large H II complexes, known in the literature as NGC 4214-I (or NW complex) and NGC 4214-II (or SE complex), located near the center of the field.
2. A number of isolated fainter knots scattered throughout the field, especially in the upper half (SW) of the images.
3. Extended, structurally amorphous Diffuse Interstellar Gas (DIG) surrounding the two main complexes and some of the isolated knots.

The ISM exhibits a wide range of structural features of various sizes, surface brightnesses, and luminosities. There are bright, compact knots; rings and incomplete shells roughly $3'' - 7''$ ($\sim 60 - 140$ pc) in diameter; and fainter, wispy filaments and arcs, whose dimensions range between roughly $5''$ and $20''$ ($\sim 100 - 400$ pc) along their longest dimension. Globally, the low surface brightness gas is patchy in the extreme outer parts while somewhat elliptical in the inner regions. Most of the high surface brightness features reside within the very inner regions, without any noticeable symmetric order. Although there are a few cases of bright outlying regions of isolated knots, the structure of the narrow band emission of NGC 4214 becomes increasingly more extended and filamentary and of lower surface brightness as one goes from the inner to the outer regions. It is, thus, natural to think of NGC 4214 as a centrally concentrated region of two large H II complexes within $15''$ or 300 pc of the center of the WFPC2 field and some fainter isolated regions. Both types of star forming units are superimposed on a more extended DIG ($> 30''$ or 600 pc), which is visible only in $\text{H}\alpha$ but not in the high excitation $[\text{O III}] \lambda 5007$ line. This type of global morphology was well noted in the past (Hodge 1969, 1975; Hunter 1982).

The morphology apparent in the radio continuum images of Fig. 6 is different at the two wavelengths. The 6 cm image shows a number of peaks which coincide with the brightest H α peaks, indicating that most of the flux is produced by thermal emission in the H II regions. The relative peak intensity among knots is not the same as in the H α images due to different amounts of extinction. On the other hand, the 20 cm image shows a morphology which is not so well correlated with H α . Even though some knots appear at the same location of the H α or 6 cm ones, there are several others with non-existent or weak counterparts at those wavelengths. In those cases most of the emission has a non-thermal origin with a more negative spectral index which causes the corresponding 6 cm emission to be weak.

The morphology in the H α continuum image of Fig. 4 is quite different from the narrow band one. There we see a number of clusters dispersed parallel to the horizontal axis of the image superimposed on a well-defined ellipsoidal background with its major axis inclined 15° with respect to that direction. A large number of individual bright stars are scattered across the whole WFPC2 field. Some of the clusters are associated with narrow band structures while others show no such correspondence. The ellipsoidal unresolved background corresponds to the old population in the bar of NGC 4214 (Fanelli et al. 1997) and the probable nucleus of the galaxy is indicated as III_s (the nomenclature is explained below). The two main complexes are not centered with respect to the ellipsoid but displaced toward the E-SE, with NGC 4214-II located further away from the nucleus than NGC 4214-I.

The individual H α knots have been identified by several authors, most recently by MMMVC, who provide in their Table 2 a list of equivalences with some of the older nomenclatures. Here we present in Table 2 a more standardized nomenclature with 13 different units and the corresponding equivalences to the one defined by MMMVC using lower resolution and coverage⁹. We decided to use a classification which was as consistent as possible with previous work and which also identified the different physical units. However, we note that with the present data it is possible that the assignment of physical character to some of the units may be uncertain and we also note that even in the high resolution HST images, there is some subjectivity in separating individual H II regions. Thus, it is possible that “well resolved” clumps may actually be a collection of a few smaller individual objects.

The first two units, NGC 4214-I and NGC 4214-II, correspond to the main H II complexes in the center of the WFPC2 field (previously, NW and SE complexes). NGC 4214-III and NGC 4214-IV are two large compact continuum sources to the left (NW). Then, NGC 4214-V to NGC 4214-XIII are progressively fainter H α structures. When appropriate, substructures within each unit are assigned a letter and named I-A, I-B and so on. If even smaller H α knots are found, they are assigned a number (and named I-A1, I-A2...). Finally, a letter n is added to the name in each entry in Table 2 if the aperture is defined with respect to the narrow line image (because it is a

⁹Those authors used a classification scheme in which numbered knots corresponded to H α maxima while lettered ones corresponded to continuum maxima.

pure nebular knot or because there is no obvious large stellar cluster associated with it) or an s if it is defined with respect to the continuum image (because it is a stellar cluster with weak or no nebular emission around it or because it encompasses the location of the cluster in a unit with extended nebular emission). No letter is added if the aperture includes one or several large stellar clusters and the nebular emission around them. This nomenclature is better explained with a few examples: I-As is a stellar cluster in NGC 4214-I with weak nebular emission at its position and surrounded by several mostly nebular features I-A1n, IA2n..., with I-A being used to refer to the whole region; II-A is a stellar cluster with intense cospatial nebular emission (thus, with no need to define II-As or II-An); NGC 4214-III is a stellar cluster with weak nebular emission if any. The position of each of the units and subunits is indicated in Figs. 2, 4, and 7, as appropriate.

We now analyze the different units in NGC 4214. For the rest of the paper, except where noted, ages are obtained from MMMVC, who use a combination of criteria ($W(H\beta)$, $W(WR \lambda 4686)$, $L(WR \lambda 4686)/L(H\beta)$, and T_{eff}) to determine them.

3.1.2. NGC 4214-I

NGC 4214-I is the largest H II complex in the galaxy and also the one with the most intricate morphology. It includes several star clusters and has a complex H α structure dominated by the presence of two cavities or intensity minima.

I-As is a massive young (3.0–3.5 Myr) Super Star Cluster (SSC) which was previously studied using HST FOC observations by Leitherer et al. (1996). Those authors find that the SSC core has a very small size (diameter $\lesssim 5$ pc) and contains several hundred O stars. The core is in the middle of an extended star population which contains another several hundred O stars and extends up to a radius of ~ 70 pc. I-As is rich in Wolf-Rayet stars and shows wide H α emission in its spectrum (Sargent & Filippenko 1991, MMMVC).

Fig. 7 shows that I-As is located in a heart-shaped H α cavity, in between the center and the upper right corner. Our images show that the size of the cavity is $9''7 = 194$ pc in the NE-SW direction and $8''0 = 160$ pc in the NW-SE direction. Little H α emission is detected inside the cavity with the exception of that coming from the SSC core and from the region immediately below and to its right (i.e. toward the East). Some of the H α emission detected from the SSC core must be the wide component previously mentioned and some may be of nebular origin (the core can also be seen in [O III] $\lambda 5007$ in Fig. 3). The rest of the H α emission may not be real but caused by the incorrect continuum subtraction at that precise point mentioned in the previous section. The weak H α emission present in the cavity shows three velocity components (MMTM), the most intense one having a velocity similar to that of the surrounding gas and the other two being displaced one toward the red and the other toward the blue. The secondary components do not show the standard velocity ellipsoid corresponding to an expanding bubble, which prompted MMTM to suggest that we are witnessing here a bipolar flow that has punctured the plane of

NGC 4214. The red secondary component has a well defined intensity maximum in the spectra of MMTM just below the core of the SSC. In our high resolution WFPC2 image (Fig. 7), we detect there the presence of two intrusions into the heart-shaped cavity which may be the source of that red component.

The H α emission surrounding I-As has a structure which shows no spherical symmetry around the SSC. At the N border (lower left) of the cavity, I-A2n is made out of an unresolved thin straight wall, which is probably the ionization front produced by I-As, and a weak compact knot. The structure at the E border, I-A4n, is distorted by the two intrusions previously mentioned but is otherwise similar. Both join almost at a right angle at the NE border of the cavity, helping define the heart shape. The S and W borders of the cavity (I-A3n, I-A1n, and I-A5n) exhibit a more complex structure. Here the border is not so well defined, with two apparent linear structures at some points and with some intense compact knots. As a matter of fact, the most intense H α knot (in peak surface brightness) in all of NGC 4214-I is located here, at the smaller of the two apertures drawn in I-A1n in Fig. 7.

I-Bs is a 3.0 – 3.5 Myr old Scaled OB Association (SOBA, Hunter 1999), a massive cluster which, as opposed to an SSC, does not show a marked central concentration. The number of O stars in I-Bs is only $\sim 30\%$ that of I-As (Maíz-Apellániz 1999, hereafter M99). Some of its stars are of Wolf-Rayet type (Sargent & Filippenko 1991). I-Bs is also located in the middle of an elongated H α cavity, though not as clearly defined as the I-As one. However, the gas inside the cavity does show the signature of an expanding shell (MMTM). Our images show that the cavity has a size of $8''.5 = 170$ pc in the NE-SW direction and $3''.0 = 60$ pc in the NW-SE direction. The H α knots which surround the cavity seem to be formed by a series of linear structures plus an intense knot (I-B1n) at its SW border. In the H α image the cavity appears to be broken between I-B1n and I-B2n. It is just to the right (SE) of this apparent hole that MMTM detect an expanding H α bubble, which could be caused by the puncture of the cavity at that point.

Two smaller clusters can be seen between I-A and I-B: I-Es and I-F. I-Es appears to have a quite compact structure, making it another SSC candidate (though probably smaller than I-As). The H α emission around it is not too intense and appears to be part of the general NGC 4214-I background. Also, the continuum colors in the MMMVC data are significantly redder than for I-As or I-Bs, indicating a greater age ($\gtrsim 10$ Myr). On the other hand, I-F must be a young cluster since there is H α emission directly associated with it and its continuum colors are similar to I-As or I-Bs.

No large cluster is seen in the I-Cn aperture and the H α emission there is probably produced by a loose group of young stars located to the SW of I-A. I-Ds is a SOBA somewhat smaller than I-Bs (M99). Much less H α emission is observed around it in comparison to I-A or I-B, with only two (I-D1n and I-D2n) or possibly three compact H α knots associated with it. I-Gn is a heavily reddened compact H α knot (MMMVC) which falls quite close to the border between the PC and WF2 chips, hindering the study of its morphology with the present data.

3.1.3. NGC 4214-II

NGC 4214-II is the second largest complex in the galaxy in size and harbors the regions with the highest peak $\text{H}\alpha$ intensity. Its morphology is quite different from that of NGC 4214-I. In the first place, there is no dominant SSC but several smaller SOBAs which are responsible for the ionization of the gas. Also, there are no large cavities present and the clusters are located very close to (or at the same position as) the most intensely $\text{H}\alpha$ emitting knots (MMMVC). Finally, no kinematic anomalies are detected here: All the $\text{H}\alpha$ profiles are gaussian at a resolution of 18 km s⁻¹, indicating that expanding shells are non-existent or too weak in comparison with the main line emission (MMTM).

II-A and II-B are the two brightest $\text{H}\alpha$ knots in NGC 4214-II. They are both located on top of SOBAs which, at the resolution of WFPC2, appear to be centered at the same positions. The centers of the knots suffer from little extinction but the $\text{H}\alpha$ emission in their surroundings is highly extinguished (MMMVC). A dust lane runs from S to N to the W of knot II-A, extending up to knot II-B. Another one separates this last knot from II-C.

The SOBA in II-B seems to be more compact than the one in II-A, which extends toward the E. There, at a distance of $\sim 3''.5$ (~ 70 pc) we find an incomplete $\text{H}\alpha$ shell which is especially prominent in $[\text{O III}] \lambda 5007$. We have reanalyzed the data of MMTM and found no kinematic anomalies in the $\text{H}\alpha$ profile at the shell position.

From the ground II-C appears to be a single, slightly extended knot and here is clearly resolved into an incomplete shell divided into two fragments, II-C1n toward the SW and II-C2n toward the NE. The diameter of the shell is $2''$ (40 pc) and the stellar cluster is located closer to the brightest of the two fragments, II-C1n. Despite the appearance of an expanding broken shell, the kinematic $\text{H}\alpha$ profile reveals a single $\text{H}\alpha$ component (MMTM).

II-Dn and II-En are two weaker $\text{H}\alpha$ knots with relatively fewer stars at their positions.

3.1.4. Other units

NGC 4214-III_s is a compact continuum source with weak associated $\text{H}\alpha$ emission. It is probably an old SSC or the nucleus of the galaxy, as suggested by the study of Fanelli et al. (1997) in the I band and the FUV. In the I band image of those authors, NGC 4214-III_s appears at the center of the weak disk of the galaxy. The H I observations of McIntyre (1998) also place the rotation center very close to NGC 4214-III_s, favoring the nuclear interpretation.

NGC 4214-IV_s has a similar appearance to NGC 4214-III_s and it also appears in the I band image of Fanelli et al. (1997). However, it is dimmer in the continuum images and here no $\text{H}\alpha$ or $[\text{O III}] \lambda 5007$ emission is detected at all except for extremely weak DIG close to the noise level which is probably unrelated to the continuum knot. NGC 4214-IV_s is probably another old SSC

or a background galaxy.

The rest of the structures visible in the $H\alpha$ image can be classified as diffuse individual knots (VII n , VIII n , IX n , XII n , XIII n), series of knots (X n , XI n) or complex $H\alpha$ knot + shell structures (V n , VI n). Some areas of those knots appear as green in Fig. 5 due to their high excitation. Finally, some very weak additional structures can be seen in the $H\alpha$ map due to the use of a logarithmic intensity scale. They are only barely above the noise level and are not visible in the $[O\ III]\ \lambda 5007$ map. Therefore, little information about them can be gained with the present data and they have not been included in the aperture list.

3.2. $[O\ III]\ \lambda 5007$ / $H\alpha$ maps

The ratio $[O\ III]\ \lambda 5007$ / $H\beta$ is one of the excitation ratios used by Baldwin et al. (1981) and Veilleux & Osterbrock (1987) to classify emission-line objects as a function of the ionizing source (photons vs. shocks) and its spectrum. For photoionized nebulae, $[O\ III]\ \lambda 5007$ originates in a region smaller than $H\beta$. The reason is that the second ionization potential of oxygen is 35.11 eV, much higher than the first ionization potential of hydrogen, 13.60 eV. The photons that can ionize O II are absorbed close to the source, producing an $[O\ III]\ \lambda 5007$ + $H\beta$ inner emitting layer while in an outer layer only $H\beta$ is produced. The $[O\ III]\ \lambda 5007$ / $H\beta$ ratio is a measure of the hardness of the spectrum: The higher the fraction of high energy ionizing photons with respect to low energy ionizing ones, the larger the first layer will be with respect to the second one and the larger the ratio. Unfortunately, there are other factors which also enter in the equation to determine the final outcome, the most important ones being the metallicity, the density, and the distance from the source to the beginning of the $[O\ III]\ \lambda 5007$ emitting layer. Therefore, even though the $[O\ III]\ \lambda 5007$ / $H\beta$ ratio can provide some useful information on the properties of the ionizing source, that information is limited unless additional data regarding the above mentioned parameters are provided.

Here we present a map formed by the division of our continuum subtracted $[O\ III]\ \lambda 5007$ and $H\alpha$ images (see Fig. 7). The data have been smoothed with a 5 pixel box before the ratio was evaluated. The areas with low signal to noise ratio have been left blank to eliminate confusion. Note that the use of $H\alpha$ instead of $H\beta$ in the denominator provides us with a better signal-to-noise ratio but is more heavily affected by extinction. Fortunately, we can distinguish between excitation and extinction effects using the $H\alpha$ / $H\beta$ maps obtained by MMMVC and M99 using ground based data, which are explained in more detail in the next section.

The excitation ratio map shows very different patterns in the two main H II complexes. In NGC 4214-II there is a generally good correlation between $H\alpha$ intensity and excitation, as previously noted by MMMVC. The five units II-A to II-En appear as excitation maxima. The highest ratio is reached in the brightest one, II-A, and it is not centered at the $H\alpha$ peak but is located between that point and the broken shell to the E previously described. High $[O\ III]\ \lambda 5007$ / $H\alpha$ values are

detected throughout most of the II-A aperture and also at the area adjacent to it toward the E. II-B also shows high excitation but in this case the maximum is located at the H α peak. II-Dn and II-En can also be detected as maxima in the excitation maps while II-C1n and II-C2n are not so well defined.

The structure of the excitation map in NGC 4214-I is more chaotic. The most obvious maximum in the ratio around I-A appears at the location of the SSC itself. However, as mentioned previously, the value of the ratio there is affected by saturation and we will not consider it here due to its questionable validity. The second obvious maximum is located at the center of the H α cavity, close to an area which appears in white due to the low value of the signal-to-noise ratio. Again, this excitation maximum may not be real and will not be analyzed here. Having said that, the most obvious real [O III] λ 5007 / H α maximum in I-A is located at the brightest H α peak, I-A1n. However, the maximum is not as marked as for II-A or II-B. In its surrounding areas, I-A3n and I-A5n, the structures in the H α image can be traced with some difficulty and that task becomes even harder in the rest of I-A.

The situation described for I-A becomes even more extreme in I-B. Here, the most intense H α knot, II-B1n not only is not a high excitation maximum but it sits at the tip of a low [O III] λ 5007 / H α finger which penetrates from the left. Even though some dust lanes exist in the area, this structure is not due to extinction since it can be seen in the low resolution maps of MMMVC. In general, the correlation between H α intensity and excitation here is very weak.

The highest excitation ratios in NGC 4214-I are found outside I-A and I-B. I-C1n shows an excitation structure and values similar to those of II-A, with high values at the H α peak and even higher values at a position nearby. Knot I-Hn shows an even higher [O III] λ 5007 / H α value and its surrounding areas toward the E are also of high excitation, even though their H α intensity is quite low. This anomaly was already detected by MMMVC, who noted that it appeared only in [O III] λ 5007 / H β but not in [N II] λ 6584 / H α or in [S II] λ 6717+6731 / H α . At this resolution, a N-S excitation ratio gradient which crosses most of NGC 4214-I can be observed.

The rest of the structures seen in the [O III] λ 5007 / H α map generally follow the same scheme described for NGC 4214-II: high excitation values correspond to H α peaks. We only note here that NGC 4214-XIIIIn shows anomalously high excitation values.

4. INTEGRATED PHOTOMETRY

4.1. WFPC2 data

We have integrated the [O III] λ 5007, H α , and H α continuum fluxes for the apertures in Table 2. The results are shown in Table 3. We also show the corresponding values of the integrated ratios, [O III] λ 5007 / H α and $W(H\alpha)$ in Table 4.

Following Maíz-Apellániz et al. (2000), we present our results using three different extinction corrections: no extinction, foreground variable dust screen, and dust-gas mixed (the validity of these models is later analyzed in the discussion). No data are presented for the continuum at $\text{H}\alpha$ using a mixed model due to the unphysical character of such an application (most of the continuum originates in stars which can have a spatial distribution along the line of sight quite different than that of the gas). For $W(\text{H}\alpha)$ several possibilities are considered: no extinction, only gas extinguished (foreground or mixed models), and both gas and stars foreground extinguished. The extinction data are taken from the MMMVC and M99 maps and have a variable resolution from $\approx 1''$ for the areas with the highest $\text{H}\alpha$ intensities to $\approx 5''$ for low intensity ones. The data cover all of NGC 4214-II, most of NGC 4214-I, and other areas of interest. Outside the coverage we have used an extinction typical of the DIG surrounding NGC 4214-I and II. Those integration areas where most of the flux is not included in the M99 maps are marked with an asterisk in Table 2 to indicate the uncertain character of the extinction correction there.

Most of the $\text{H}\alpha$ and $[\text{O III}] \lambda 5007$ emission comes from NGC 4214-I and NGC 4214-II. Table 3 reveals the large uncertainty caused by the distribution of dust with respect to gas. The correction due to extinction applied to all of NGC 4214 more than doubles for both $\text{H}\alpha$ and $[\text{O III}] \lambda 5007$ when we consider a mixed model instead of a foreground screen. In some cases it is so large that the real values of the fluxes are extremely uncertain. Such is the case for I-A1n, I-A3n, I-Gn, II-A and II-B. The most extreme case is I-Gn. There we are at the point of the extinction curve where the $\text{H}\alpha / \text{H}\beta$ ratio cannot give a good estimate of the real extinction if dust and gas are mixed (Maíz-Apellániz et al. 2000).

The $[\text{O III}] \lambda 5007 / \text{H}\alpha$ data in Table 4 reveal that, in general, NGC 4214-II has a higher excitation than NGC 4214-I. An excitation gradient appears to be present in NGC 4214-II with high values to the right (II-A) and low ones to the left (II-C). In I-A high excitation values are found only in the compact knot in I-A1n and, to a lesser degree, in the one in I-A3n. The excitation in I-B is even lower than in I-A. In other regions of NGC 4214-I we find high excitation in I-C1n, I-Gn, and I-Hn.

Several isolated $\text{H}\alpha$ knots exhibit stronger than expected excitation values. We have already mentioned the cases of I-Hn and XIIIIn, but the same is also true for V-An, VI-An, and XIIIn (the high value of NGC 4214-IVs is artificially produced by the low signal to noise ratio of the emission lines and the incorrect continuum subtraction there). The most extreme cases are V-An and XIIIIn, where the reddened value of $[\text{O III}] \lambda 5007 / \text{H}\alpha$ is higher than 1.5.

The equivalent width of the Balmer lines can be used to estimate the age of a star-forming knot (see, e.g. Cerviño & Mas-Hesse 1994). However, there are several problems that complicate the age estimation, namely, the choice of a consistent aperture, the differential reddening, and the presence of an underlying old population (MMMVC). Here the two first problems can be easily solved while for the last one we can resort to the estimates of MMMVC. To establish the correspondence we use the models of Cerviño et al. (2000) and Leitherer et al. (1999) to plot in Figure 8 the relation between

age and $W(\text{H}\alpha)$. The differences between the predictions are caused mainly by the assumptions about the number of hydrogen-ionizing photons which are absorbed by dust or escape (0% in the Leitherer et al. (1999) models and 30% in the Cerviño et al. (2000) ones), and in the use of different stellar atmospheres.

The expected values for $W(\text{H}\alpha)$ are $1000 - 2500$ Å for very young clusters (age $\lesssim 3$ Myr) and $500 - 1000$ Å for ages in the range between 3 and 4 – 5 Myr. This predicted decrease in $W(\text{H}\alpha)$ does not take into account the morphological evolution caused by mechanical energy deposition, since the fraction of effective to emitted ionizing photons is kept constant, as mentioned previously. Given that the surrounding gas is dispersed in a timescale comparable to 5 Myr, in a realistic scenario the decrease would probably be even more pronounced.

Values very close to or higher than 1000 Å are found for all the knots in NGC 4214-II except for II-C1n and II-C2n, indicating the very small age of this complex, as already pointed by MMMVC. The lower $W(\text{H}\alpha)$ values, broken shell appearance, and detection of nebular He II emission in II-C (probably caused by extreme WR stars, Schaerer & Vacca 1998) point toward a slightly greater age for this knot. The overall value of the $W(\text{H}\alpha)$ for NGC 4214-II is quite lower than 1000 Å due to the existence of an underlying population which is responsible for about $\sim 50\%$ of the $\text{H}\beta$ continuum (MMMVC). When that effect is taken into account, the measured estimated age for NGC 4214-II assuming a single burst model is consistent with 2.5 – 3.0 Myr.

The $W(\text{H}\alpha)$ values for NGC 4214-I are in general lower than those of NGC 4214-II. When the underlying population is taken into account, an average age in the 3.0 – 4.0 Myr range is the most plausible estimate. However, the two small apertures centered at knots I-A1n and I-A3n show values similar to those of the knots in NGC 4214-II, pointing toward a smaller age.

4.2. Radio data

The lower resolution (4" in each band) and signal to noise of the radio data does not allow us to use the apertures of the analysis of the previous section. However, five distinct knots are visible in the 6 cm and/or 20 cm maps and we have used those as reference points for the radio apertures. Two of the five apertures are located in NGC 4214-II, with each one of them roughly corresponding to its SE (II-AE) and NW (II-BCD) halves. The other three apertures are located in NGC 4214-I, roughly centered at the position of the I-A, I-F, and I-B WFPC2 apertures. We show in Table 5 the integrated radio fluxes for the five apertures with the corresponding spectral index α .

The spectral index of II-AE is almost exactly 0.1, the value expected for a young (< 3 Myr) star-forming knot with only thermal radio emission (Mas-Hesse 1992). II-AE is the brightest knot of all NGC 4214 at this resolution in the 6 cm image but only the third in the 20 cm map, which is consistent with such a high spectral index. The spectral index of II-BCD is not as high, indicating that the radio emission is a mixture of thermal and non-thermal emission. Looking at Fig. 6, we can see that the 6 cm emission appears to originate from a point source toward the SE side of the

aperture while the 20 cm emission is more elongated toward the north. This is an indication that most of the thermal emission is coming from knots II-B and II-Dn while most of the non-thermal emission is originating in II-C.

The spectral index of I-A is also quite high, indicating a predominantly thermal origin of the emission. The position is consistent with an origin in knot I-A1n and, to a lesser extent, I-A3n. However, a non-negligible fraction is non-thermal and may be originating at knot I-A1n or at the nearby SSC. The emission coming from the other two radio apertures has much lower spectral indices. Even though some thermal emission may be originating from knots I-B1n and I-B2n, undoubtedly most of the radio flux detected there is non-thermal and concentrated on the two knots clearly visible in the 20 cm image. The weaker of the two non-thermal sources is centered close to the I-Bs cluster and extends toward the SE. Its extent follows the approximate location of the superbubble detected by MMTM which is expanding into the intercloud medium.

The stronger non-thermal source is located within 2" of the stellar cluster in the WFPC2 aperture I-F but the resolution of the VLA data does not allow us to determine if they are spatially coincident. It has the lowest spectral index in NGC 4214 and we identify it as a supernova remnant. We have reanalyzed the data in MMMVC and MMTM and discovered clear signals of the nature of this object. First, it appears as a well differentiated knot in the [N II] $\lambda 6584$, [S II] $\lambda 6717$, and [S II] $\lambda 6731$ maps but not in the H α , H β , [O III] $\lambda 5007$, or He I $\lambda 6678$ ones (see Fig. 3 of MMMVC). Second, a wide ($\sigma = 60 - 65 \text{ km s}^{-1}$) component appears in all of the analyzed emission lines, as is shown in Fig. 9. The center of the wide component is displaced by $\approx 10 \text{ km s}^{-1}$ toward the red with respect to the nebular emission. Finally, as shown in Table 6, the wide component is the one responsible for the localized high values of the [S II] $\lambda 6717+6731$ and [N II] $\lambda 6584$ emission. Note that the [O III] $\lambda 5007$ / H β ratio is not too different from the ambient nebular emission, which makes the SNR hard to detect with our WFPC2 data. The position of the wide component in the long-slit data is also compatible with that of the cluster in I-F but, again, the spatial resolution is not good enough to make a certain identification. We have also looked in the ROSAT archive and found an HRI image of NGC 4214, but no strong x-ray source can be observed at this location.

Some radio emission originating outside the two main H II complexes can be observed in the upper right quadrant of Fig. 6. One knot appears to be thermal emission associated with NGC 4214-VIn. The knot located above it and the group to its right do not show up in the 6 cm image and are likely non-thermal sources. Thermal emission from knots VIIIn, VIIIn, or IXn is not detected.

The ratio of thermal radio emission to H α can be used to calculate the true optical depth τ_{rad} at H α caused by dust (see, e.g. Churchwell & Goss 1999):

$$\tau_{\text{rad}} = \ln \left[1.27 \cdot 10^9 \left(\frac{T_e}{10^4 \text{ K}} \right)^{0.59} \left(\frac{\nu}{10^9 \text{ Hz}} \right)^{-0.1} \frac{F_\nu(\text{Jy})}{F(\text{H}\alpha)(\text{erg s}^{-1} \text{ cm}^{-2})} \right], \quad (3)$$

where T_e is the electron temperature and ν is the frequency at which the radio continuum flux, F_ν , is measured. For NGC 4214, $T_e = 10\,500$ K (Kobulnicky & Skillman 1996), and for $\nu = 4.885$ GHz (this choice of frequency will become obvious in the next paragraph) we obtain:

$$\tau_{\text{rad}} = \ln \left[\frac{F_\nu(\text{Jy})}{F(\text{H}\alpha)(\text{erg s}^{-1} \text{ cm}^{-2})} \right] - 20.83. \quad (4)$$

Equation 3 is not a strong function of temperature. For example, changing T_e by 1 000 K produces a change of only 0.05 or 0.06 in τ_{rad} . The largest uncertainty by far when using this equation is discerning the contribution of non-thermal emission to the radio continuum. To do that, we assume the presence of a thermal component with spectral index $\alpha_T = 0.1$ and of a non-thermal one with spectral index α_{NT} (Sramek & Weedman 1986) and use our measured values of α to assign which fraction of the radio continuum corresponds to each one of them. Unfortunately, the value of α_{NT} can be as high as ≈ -0.6 and as low as ≈ -1.4 . Therefore, only when α is close to -0.1 can τ_{rad} be accurately determined.

We show our values of τ_{rad} measured from Eq. 3 in Table 5 for three of the radio apertures. We have not attempted to measure τ_{rad} at the other two apertures due to dominance of non-thermal emission there. Two values are given for I-A and II-BCD considering the two possibilities for α_{NT} , while only one is given for II-AE since the non-thermal contribution there is negligible. The measured H α flux used to calculate τ_{rad} is also shown for those apertures in Table 5 and was obtained from the WFPC2 data after the resolution was matched to that of the radio data. The H α flux corrected for extinction using the Balmer ratio data of M99 and a foreground screen model is also shown, and from the logarithm of the ratio of the two quantities we obtain τ_{rad} as measured using the Balmer ratio.

In the three cases we find that τ_{rad} is significantly higher than τ_{Bal} (the apparent optical depth at H α as measured from the Balmer ratio), which indicates that the uniform foreground screen model is not valid in this case, as already found for other star-forming regions (Maíz-Apellániz et al. 2000 and references therein). We will analyze the significance of this result later on. We only point out here that the value of τ_{rad} is the real mean optical depth at H α and that it is independent of the resolution of the data as long as all the fluxes are included. On the other hand, the value of τ_{Bal} can be heavily weighted toward low-extinction areas (holes in the foreground screen or skin emission from dusty H II regions) and that its value is resolution dependent.

5. DISCUSSION

The WFPC2 nebular images of NGC 4214 presented here are an illuminating example of the complex morphology of the ionized gas around regions with intense star formation. This complexity is sometimes overlooked when more distant unresolved objects are studied.

5.1. Sources and sinks of ionizing photons

The balance between sources and sinks of ionizing photons in the ISM is not completely understood. Regarding the sources, several problems exist: the estimation of the ionizing flux as a function of initial mass, the detection of the massive stars hidden in their dust enshrouded cocoons (Drissen et al. 2000), and the precise measurement of stellar masses around the high mass end of the IMF (Antokhina et al. 2000). Of those problems, the most serious one is the first one: the extreme opacity of the ISM below 912 Å hampers the direct measurement of the ionizing fluxes of O and B stars. Even though a lot of effort has been made in the modelling of the ionizing fluxes, the strong winds in the atmospheres of those stars and other complications make the results somewhat uncertain (see, e.g., Schaerer & de Koter 1997). At the present time it has been possible to analyze the ionizing flux from only two B stars, β and ε CMa, with somewhat contradictory results (Cassinelli et al. 1995, 1996), and no direct measurements exist for spectral type O. Therefore, it is not clear how many ionizing photons are emitted even in the case of well studied H II regions.

Regarding the sinks of the ionizing photons three major questions remain to be answered completely: What fraction of the ionizing photons is (a) destroyed by dust, (b) not absorbed locally but in the rest of the galaxy, (c) escape from the galaxy? That dust plays a large role in the interaction of the ionizing flux with the ISM is readily apparent in the HST images of M16 (Hester et al. 1996). With respect to the fraction of photons that are absorbed elsewhere in the galaxy (to form the DIG), several studies place it close to 40% independent of the Hubble type (Greenawalt et al. 1998 and references therein). The number of photons which actually escape is more difficult to measure and only a small sample has been studied. The results indicate that the fraction is quite small (Leitherer et al. 1995).

Our images of NGC 4214 show that the number of ionizing photons escaping from an H II region can be highly variable. The solid angle covered by the surrounding dense gas around the SSC I-As is certainly not large and, even though our three dimensional information is not complete, it is clear from the geometry that more than half of the ionizing photons from the SSC itself are not absorbed by the nearby surrounding gas but must escape to large distances, preferentially along directions close to the line of sight (towards or away from us). Furthermore, the low extinction observed in the UV (Mas-Hesse & Kunth 1999) and the likely puncture of the galactic disk revealed by kinematic data (MMTM) suggest that a significant fraction of the ionizing flux may be escaping to the intergalactic medium. On the other hand, the dense clouds of gas which exist around the ionizing clusters of II-A and II-B make it more difficult for the Lyman continuum photons to escape far away and most of them should be contributing to the formation of Balmer lines close to their sources or be destroyed by dust. With respect to the other massive clusters, I-Ds has even less gas around it than I-As while II-C and I-Bs are in an intermediate situation between II-A or II-B and I-As.

Knots II-A and II-B are thus prototypes of massive compact H II regions with core sizes of $\lesssim 20$ pc for the H α emission. They are also distinguished by their high values of [O III] $\lambda 5007$ /

$\text{H}\alpha$ and $W(\text{H}\alpha)$, the high dust content of their immediate surroundings, and the gaussian profile of their emission lines. As we have seen in the previous section, the high values of $W(\text{H}\alpha)$ indicate a small ($\lesssim 3$ Myr) age. These properties indicate that the gas is being ionized *in situ*, as we will discuss in more detail afterwards. Two other knots in NGC 4214 show very similar characteristics, the ones located in the small I-A1n and I-A3n apertures. They are clearly differentiated from their surroundings by their point-like character (as opposed to the filamentary structures around them), high intensity contrast, and excitation. They are also located next to dust clouds and the velocity profiles of their emission lines is gaussian. The main difference between these knots and the ones in NGC 4214-II is that they are not located on top of the most massive cluster in the area (I-As), but at some distance from it (60 pc in projection for the knot in I-A1n and 120 pc for I-A3n). However, the similarities in the observed properties indicate that the central knots in I-A1n and I-A3n are ionized *in situ* and not by the SSC. This is supported by the fact that they cover relatively small solid angles as seen from I-As ($\approx 1.9\%$ and 0.5% , respectively, if they all are in the same plane perpendicular to the line of sight and are spherically symmetric), but contain four to eight times more of the fraction of the total $\text{H}\alpha$ flux in NGC 4214 I-A ($8 - 11\%$ and $2.5 - 4.0\%$, respectively) and six to eleven times of the $[\text{O III}] \lambda 5007$ flux ($12 - 19\%$ and $3.0 - 5.5\%$, respectively). This situation is quite similar to the one found in N11 in the LMC (Parker et al. 1992; Walborn & Parker 1992), where an ≈ 4 Myr old cluster has triggered the formation of a second cluster at the present $\text{H}\alpha$ maximum. Those authors coined the term *two-stage starburst* to describe such an event, because the disruption of the ISM produced by the first cluster appears to be the cause for the formation of the second one. We propose here that I-As + (I-A1n + I-A3n) could be such an event, but certainty cannot be reached unless UV spectroscopy of the individual knots is obtained. Other examples of multi-stage starbursts in nearby galaxies are analyzed in González-Delgado et al. (1997) and Leitherer (1998) and references therein.

We present in Table 7 the $\text{H}\alpha$ and $[\text{O III}] \lambda 5007$ fluxes binned as a function of pixel flux. We established the limit between the DIG and the H II regions by averaging $\text{H}\alpha$ and $[\text{O III}] \lambda 5007$ and making intensity cuts as a function of position for different knots. We then determined that the change of slope at the border of the H II regions takes place at $\approx 0.3 \cdot 10^{-16}$ erg s $^{-1}$ cm $^{-2}$ for most cases. Thus, the sum of the first two bins corresponds to the percentage of the emission originating in the DIG and the value obtained (42% for $\text{H}\alpha$ and 37% for $[\text{O III}] \lambda 5007$) is similar to that of other galaxies.

The diffuse ionized gas is preferentially distributed in two areas adjacent to the main H II complexes: (a) in between the two complexes, to the S of NGC 4214-I and W of NGC 4214-II (around I-Hn); and (b) at the N border of NGC 4214-I. The value of $[\text{O III}] \lambda 5007 / \text{H}\alpha$ in these two regions is quite different: in the first case we have already mentioned that high values are found (the integrated value for the I-Hn aperture is close to 1.5, even higher than the integrated value for NGC 4214-II), while the second area has lower excitation values, in the range (0.6-0.8) typical of most of the DIG in NGC 4214. What is the origin of this difference? The most likely explanation is that in the first area a population of dispersed OB stars is contributing most of the

ionizing photons, thus providing a nearby source, while in the second area the ionizing source is farther away (probably the stars in I-Ds as well as some leakage from the rest of NGC 4214-I). The difference in distance to the source could cause the change in ionization parameter needed to explain the different excitation ratios. This possibility will be further explored in Paper II.

5.2. Bubbles and kinematic ages

A morphological evolution is readily apparent in our WFPC2 images of NGC 4214. The H II regions around young clusters like II-A and II-B are compact and filled while the ones around older clusters like I-As and I-Bs are much larger and have been evacuated in their central parts. An intermediate case, where a small bubble can be observed around the cluster, is seen in II-C while older clusters like I-Ds have little gas around them. This evolutionary trend is consistent with the morphology observed in other nearby massive H II regions like NGC 604 or NGC 2363.

Qualitatively, this evolution is easily explained by the deposition of kinetic energy into the surrounding ISM by massive stars in the form of winds and supernova explosions. The quantitative predictions of the models have been compared with observations of clusters with a few O stars in the LMC by Oey (1996), but relatively little effort has been made to verify them for more massive (and generally more distant) clusters. The extrapolation of the classic treatment of wind bubbles created by single stars of Weaver et al. (1977) to massive clusters yields a surprising result: given the weak dependence of the size of the bubble R on the input kinetic energy luminosity L_k and the surrounding medium density n_0 ($R \propto (L_k/n_0)^{0.2}t^{0.6}$), R should be almost solely dependent on t for a wide variety of circumstances. For 2-4 Myr old clusters with the number of massive stars typical of the ones described in this paper R should be in the range of 50 to 125 pc. MMTM used ground-based data to show that the bubbles around I-As and I-Bs were smaller than expected while the ones around the clusters in NGC 4214-II could not be observed.

With our higher resolution WFPC2 data we confirm that the sizes of the bubbles around I-As and I-Bs are indeed smaller than expected by $\approx 30\%$ (corresponding to a kinematic age smaller by $\approx 50\%$). What is more surprising is the absence of an apparent bubble around II-A and II-B (even with a pixel size of 2 pc) and the small size of the one detected around II-C ($R \approx 20$ pc). This discrepancy is in the same direction as the one detected by Oey (1996) for smaller clusters in the LMC. The NGC 4214 results cannot be explained by changing the number of stars, the value of n_0 , or the age of the cluster and, therefore, we must conclude that the model of Weaver et al. (1977) is not applicable in these cases.

The explanation of this effect may lie in the pressurized character of the cores of the molecular clouds where massive clusters form. The external pressure slows down the expansion of the wind-blown cavities around individual stars and can restrict them to $\lesssim 1$ pc sizes during their first 1-2 Myr. For isolated stars, this phase is known as the ultracompact H II region stage and may be quite long lasting, since it is possible for them to reach a stable state (García-Segura & Franco

1996). For compact clusters, however, the situation must be different. The high number of bubbles created and the internal motion of the stars must end up producing a superbubble which is rapidly thermalized by wind-wind interactions. This superbubble would finally be able to break out of the cocoon but only after ≈ 2 Myr have elapsed since the formation of the cluster.

This 2-3 Myr delay would nicely fit the observations described in this paper as well as those made for other nearby massive clusters. For example, R136 is located at the center of an incomplete $R \approx 10$ pc H II shell which is the brightest H α structure in 30 Doradus and probably delimits the extension of the cavity created by the cluster. The incomplete shell traces the photoevaporating surface of the surrounding high density gas (Scowen et al. 1998), where a very young triggered second generation is already found (Walborn et al. 1999). The age of R136 is close to 2 Myr (Walborn & Blades 1997; Massey & Hunter 1998), so the size of the superbubble predicted by the Weaver et al. (1977) model should be an order of magnitude larger. However, if we include a 2 Myr delay the observations can be easily reproduced since a 10 pc superbubble can be formed in a timescale of one or a few hundred thousand years.

It appears then that the clusters in NGC 4214-II may be at a similar stage to that of R136. However, the kinematics of the warm ionized gas in 30 Doradus is extremely complicated with many kinematic components (Chu & Kennicutt 1994), while that of NGC 4214-II is much simpler, with only single component gaussians (MMTM). The reason for this difference is probably twofold: (1) The 30 Doradus region appears to have had a complicated star formation history in the past 10 Myr (Walborn & Blades 1997). Thus, the behavior of the warm ionized gas should be dominated not by the kinetic energy input from R136 but from that of the previous star-forming episodes. (2) When examined in detail, the high intensity H α emitting areas may not be so different after all. The high spatial and spectral resolution data of Melnick et al. (1999) reveal that the velocity profile of the 10 pc shell around R136 (the F in their Figure 1; note that the figure does not have an aspect ratio of unity) is one of the only ones in 30 Doradus which is approximately gaussian. This is what would be expected of a photoevaporating surface but not of a rapidly expanding shell or shell fragment (Tenorio-Tagle et al. 1996). Therefore, an H α velocity profile of 30 Doradus stripped of the high velocity components energized by previous star-forming episodes may not be so different from that of NGC 4214-II.

5.3. Where is the dust?

The distribution of the dust in a massive H II region with respect to the gas and the stars, and the final effect it has on the measured radiation field is not very clear. A simple star-like extinction model does not work because of the extended nature of the line emission and because the proximity between the scattering particles and the source can remove photons from the observed beam but also bring them back in. Some authors have proposed the use of the term attenuation in such a case instead of extinction to differentiate the two phenomena. Fanelli et al. (1988) found that the UV continuum was not as strongly affected by dust as it is in standard extinction laws for

a given reddening measured from the Balmer lines. Calzetti et al. (1994) derived an attenuation law comparing optical and ultraviolet starburst spectra based on those results. The reason for the discrepancy is easily seen in a case like I-A in NGC 4214. Even though the cause of the UV continuum and the Balmer lines is the same (the existence of massive stars), their spatial distributions are very different. Therefore, the amount of dust present around each of the sources and between them and us can also be very different. If the dust were located far away from the object, the variations would be random; in some cases there would be more dust present in front of the UV continuum sources than in front of the ionized gas, and in other cases the opposite would be true. However, if the dust were associated with the object, since the massive stars can evaporate (with their photons) and sweep (with their winds) the dust grains, there would be less dust in front of the stars than in front of the gas. Furthermore, a second generation of stars can be produced in the swept-up gas 2–3 Myr after the formation of the main 3–5 Myr old burst (Parker et al. 1992; Walborn & Parker 1992). The ionizing photons from those younger stars can provide a significant contribution to the total number of optical nebular photons emitted (since there is plenty of gas around them and early O stars have not yet disappeared) while being very hard to detect in the UV.

The processes described in the previous paragraph are the physical explanation of the Calzetti et al. (1994) law. However, as we have seen, the younger massive H II regions may not have had enough time to create a superbubble around the cluster and in that case the Calzetti et al. (1994) law should not be applicable.

Maíz-Apellániz et al. (2000) give the expected values of τ_{Bal} and τ_{rad} for three dust-gas configurations: uniform screen, patchy screen, and dust-gas mixed. Our combination of radio and optical data shows that a uniform dust screen model can not reproduce the observed values. A model with dust and gas uniformly mixed gives a better fit but, in general, τ_{rad} is too large for a given τ_{Bal} , specially for the case of II-BCD. This is not surprising, given the existence of large structural non-uniformities inside the apertures used, as evidenced by the WFPC2 images. For the II-BCD aperture, the long-slit data of MMMVC indicate that we are including two regions (II-BD vs. II-C) with different attenuations, so the departure from the uniformly mixed model is larger than for II-AE or I-A, where most of the Balmer emission is coming from a more homogeneous source. This is especially true for II-AE, where the uniformly mixed model gives a reasonably good fit. Therefore, we can conclude that a significant fraction of the observed dust (and maybe most of it) is physically associated with the ionized gas and is not located far away from it. This result agrees with the detection in NGC 4214 by MMMVC of small localized sources of *bluened* (i.e. with an $\text{H}\alpha / \text{H}\beta$ ratio lower than 2.86) Balmer radiation close to highly reddened sources.

This result agrees with the values observed in different parts of NGC 604 by Maíz-Apellániz et al. (2000) and with the ones obtained by Caplan & Deharveng (1986) for a number of H II regions in the LMC in the sense that a uniform screen cannot explain the measured optical and radio properties. The real optical depths at $\text{H}\alpha$ appear to be larger by 0.5 to 1.0 than the ones measured from the Balmer ratio. In the case of NGC 5253, the difference appears to be even larger

(Calzetti et al. 1997). Therefore, a measurement of the number of ionizing photons obtained by measuring H α and correcting for extinction with H β may be underestimated by a factor of ≈ 2 or even more. This source of uncertainty should be taken into account when studying unresolved galaxies located much farther away than NGC 4214.

6. CONCLUSIONS

We have analyzed WFPC2 and VLA images of NGC 4214. The main results we have obtained can be summarized as follows:

- A morphological evolution is observed in the star-forming knots of NGC 4214 from filled compact H II regions to shell-like objects to low intensity diffuse knots.
- Parallel to the morphological one, a similar evolution in the excitation ratios is detected as a function of age.
- A SNR has been discovered from the radio and optical data.
- A two-stage starburst candidate has been detected.
- The DIG in NGC 4214 contributes $\approx 40\%$ of the total H α and [O III] $\lambda 5007$ emission of the galaxy.
- The pressurized character of the molecular cloud cores apparently inhibits the formation of superbubbles around massive clusters for ≈ 2 Myr.
- Most of the dust detected in NGC 4214 by light attenuation around massive clusters is physically associated with the ionized gas.
- The number of ionizing photons obtained from integrated optical spectra of galaxies similar to NGC 4214 may be underestimated by a factor of two due to the invalidity of the foreground screen approximation for the reddening correction.

The authors would like to thank Miguel Cerviño for his help with the evolutionary synthesis models, Antxón Alberdi and Greg Taylor for their help with the VLA data analysis and J. Miguel Mas-Hesse for his useful insights on NGC 4214. We would also like to thank Richard Burg, Rosemary F.G. Wyse, and Richard E. Griffiths for encouragement and stimulating conversations. Finally, we would like to thank Claus Leitherer and an anonymous referee for the useful comments which helped improve this paper. Support for this work was provided by NASA through grant GO-06569.01-95A from the Space Telescope Science Institute, Inc., under NASA contract NAS5-26555.

REFERENCES

Allsopp, N. J. 1979, MNRAS, 188, 765

Antokhina, E. A., Moffat, A. F. J., Antokhin, I. I., Bertrand, J.-F., & Lamontagne, R. 2000, ApJ, 529, 463

Baldwin, J. A., Phillips, M. M., & Terlevich, R. 1981, PASP, 93, 5

Burg, R. I. 1987, Ph.D. thesis, Massachusetts Institute of Technology

Calzetti, D., Kinney, A. L., & Storchi-Bergmann, T. 1994, ApJ, 429, 582

Calzetti, D., Meurer, G. R., Bohlin, R. C., Garnett, D. R., Kinney, A. L., Leitherer, C., & Storchi-Bergmann, T. 1997, AJ, 114, 1834

Caplan, J., & Deharveng, L. 1986, A&A, 155, 297

Cassinelli, J. P., et al. 1995, ApJ, 438, 932

Cassinelli, J. P., et al. 1996, ApJ, 460, 949

Cerviño, M., & Mas-Hesse, J. M. 1994, A&A, 284, 789

Cerviño, M., Mas-Hesse, J. M., & Kunth, D. 2000, in preparation

Chu, Y.-H., & Kennicutt, R. C., Jr. 1994, ApJ, 425, 720

Churchwell, E., & Goss, W. M. 1999, ApJ, 514, 188

Drissen, L., Roy, J.-R., Robert, C., Devost, D., & Doyon, R. 2000, AJ, 119, 688

Fanelli, M. N., O'Connell, R. W., Robert, W., & Thuan, T. X. 1988, ApJ, 334, 665

Fanelli, M. N., et al. 1997, ApJ, 481, 735

García-Segura, G., & Franco, J. 1996, ApJ, 469, 171

González-Delgado, R. M., Leitherer, C., Heckman, T., & Cerviño, M. 1997, ApJ, 483, 705

Greenawalt, B., Walterbos, R. A. M., Thilker, D., & Hoopes, C. G. 1998, ApJ, 506, 135

Heckman, T. M., Robert, C., Leitherer, C., Garnett, D. R., & van der Rydt, F. 1998, ApJ, 503, 646

Hester, J. J., et al. 1996, AJ, 111, 2349

Hodge, P. W. 1969, ApJ, 156, 847

Hodge, P. W. 1975, ApJ, 201, 556

Hopp, U., Schulte-Ladbeck, R. E., Greggio, L., & Crone, M. M. 2000, in Spectrophotometric Dating of Stars and Galaxies (to be published)

Huchra, J. P., Davis, M., Latham, D., & Tonry, J. 1983, *ApJS*, 52, 89

Hunter, D. A. 1982, *ApJ*, 260, 81

Hunter, D. A. 1999, in Wolf-Rayet Phenomena in Massive Stars and Starburst Galaxies, K.A. van der Hucht, G. Koenigsberger and P. R. J. Eenens (eds.), Proc. IAU Symposium No. 193 (San Francisco: ASP), 418

Kobulnicky, H. A., & Skillman, E. D. 1996, *ApJ*, 471, 211

Kurucz, R. L. 1979, *ApJS*, 40, 1

Leitherer, C. 1998, in The Stellar Initial Mass Function (38th Herstmonceux Conference), 61

Leitherer, C., Ferguson, H. C., Heckman, T. M., & Lowenthal, J. D. 1995, *ApJ*, 454, L19

Leitherer, C., Goldader, J. F., González Delgado, R. M., Robert, C., Kune, D. F., de Mello, D. F., Devost, D., & Heckman, T. M. 1999, *ApJS*, 123, 3

Leitherer, C., Vacca, W., Conti, P. S., Filippenko, A. V., Robert, C., & Sargent, W. L. W. 1996, *ApJ*, 465, 717

Lejeune, T., Buser, R., & Cuisinier, F. 1997, *A&AS*, 125, 229

Maíz-Apellániz, J. 1999, Ph.D. thesis, Universidad Complutense de Madrid (M99)

Maíz-Apellániz, J., Mas-Hesse, J. M., Muñoz-Tuñón, C., Vílchez, J. M., & Castañeda, H. O. 1998, *A&A*, 329, 409 (MMMVC)

Maíz-Apellániz, J., Muñoz-Tuñón, C., Tenorio-Tagle, G., & Mas-Hesse, J. M. 1999, *A&A*, 343, 64 (MMTM)

Maíz-Apellániz, J., Pérez, E., & Mas-Hesse, J. M. 2000, in preparation

Mas-Hesse, J. M. 1992, *A&A*, 253, 49

Mas-Hesse, J. M., & Kunth, D. 1991, in Wolf-Rayet Stars and Interrelations with Other Massive Stars in Galaxies, K. A. van der Hucht and B. Hidayat (eds.), Proc. IAU Symposium No. 43 (Dordrecht: Kluwer Academic Publishers), 613

Mas-Hesse, J. M., & Kunth, D. 1999, *A&A*, 349, 765

Massey, P., & Hunter, D. A. 1998, *ApJ*, 493, 180

McIntyre, V. J. 1998, *PASA*, 15, 157

Melnick, J., Tenorio-Tagle, G., & Terlevich, R. 1999, MNRAS, 302, 677

Meynet, G., Maeder, A., Schaller, G., Schaerer, D., & Charbonnel, C. 1994, A&AS, 103, 97

Mihalas, D. 1972, Non-LTE model atmospheres for B and O stars, NCAR-TN/STR-76

Oey, M. S. 1996, ApJ, 467, 666

Parker, J. W., Garmany, C. D., Massey, P., & Walborn, N. R. 1992, AJ, 103, 1205

Sargent, W. L. W., & Filippenko, A. V. 1991, AJ, 102, 107

Schaerer, D., Charbonnel, C., Meynet, G., Maeder, A., & Schaller, G. 1993, A&AS, 102, 339

Schaerer, D., Contini, T., & Pindao, M. 1999, A&AS, 136, 35

Schaerer, D., & de Koter, A. 1997, A&A, 322, 598

Schaerer, D., de Koter, A., Schmutz, W., & Maeder, A. 1996, A&A, 310, 837

Schaerer, D., & Vacca, W. D. 1998, ApJ, 497, 618

Schmutz, W., Leitherer, C., & Gruenwald, R. 1992, PASP, 104, 1164

Scowen, P. A., et al. 1998, AJ, 116, 163

Sramek, R. A., & Weedman, D. W. 1986, ApJ, 302, 640

Tenorio-Tagle, G., Muñoz-Tuñón, C., & Cid-Fernandes, R. 1996, ApJ, 456, 264

Thronson, H. A., Hunter, D. A., Telesco, C. M., Greenhouse, M., & Harper, D. A. 1988, ApJ, 334, 605

Veilleux, S., & Osterbrock, D. E. 1987, ApJS, 63, 295

Walborn, N. R., Barbá, R. H., Brandner, W., Rubio, M., Grebel, E. K., & Probst, R. G. 1999, AJ, 117, 225

Walborn, N. R., & Blades, J. C. 1997, ApJS, 112, 457

Walborn, N. R., & Parker, J. W. 1992, ApJ, 399, L87

Weaver, R., McCray, R., Castor, J., Shapiro, P., & Moore, R. 1977, ApJ, 218, 377

Whitmore, B., Heyer, I., & Casertano, S. 1999, PASP, 111, 1559

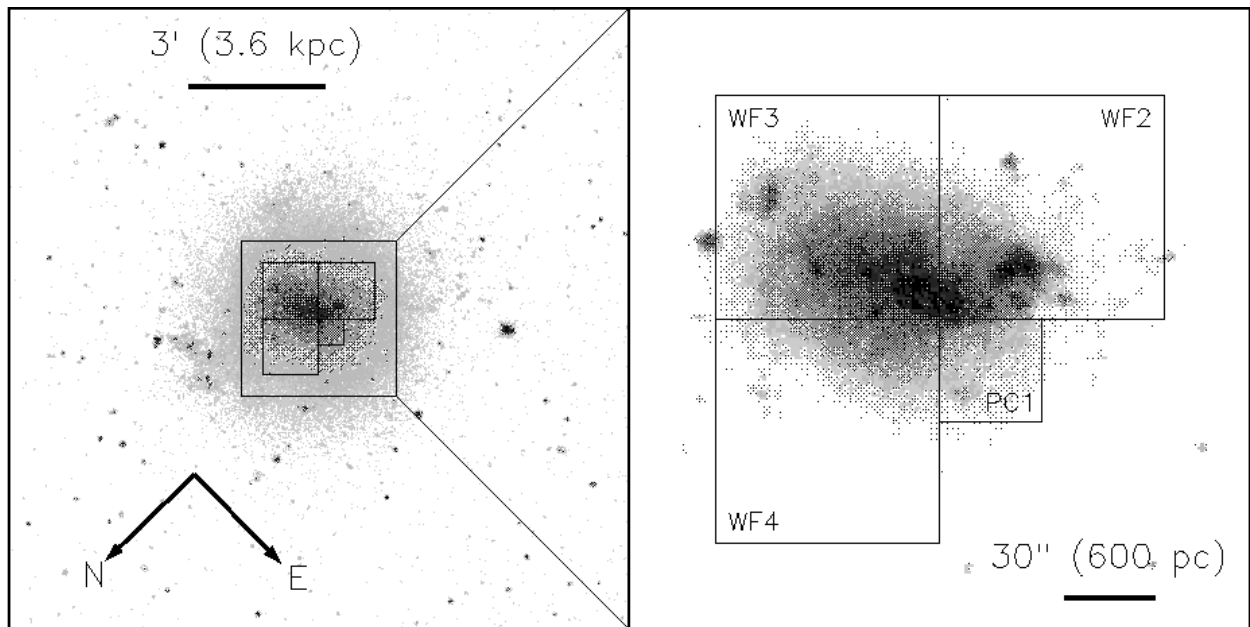


Fig. 1.— Digitized Sky Survey image of NGC 4214 with the WFPC2 field superimposed on it. The contrast in the large scale image on the left is stretched to show the low brightness disk of the galaxy while the one in the blow-up on the right yields a more realistic perception.

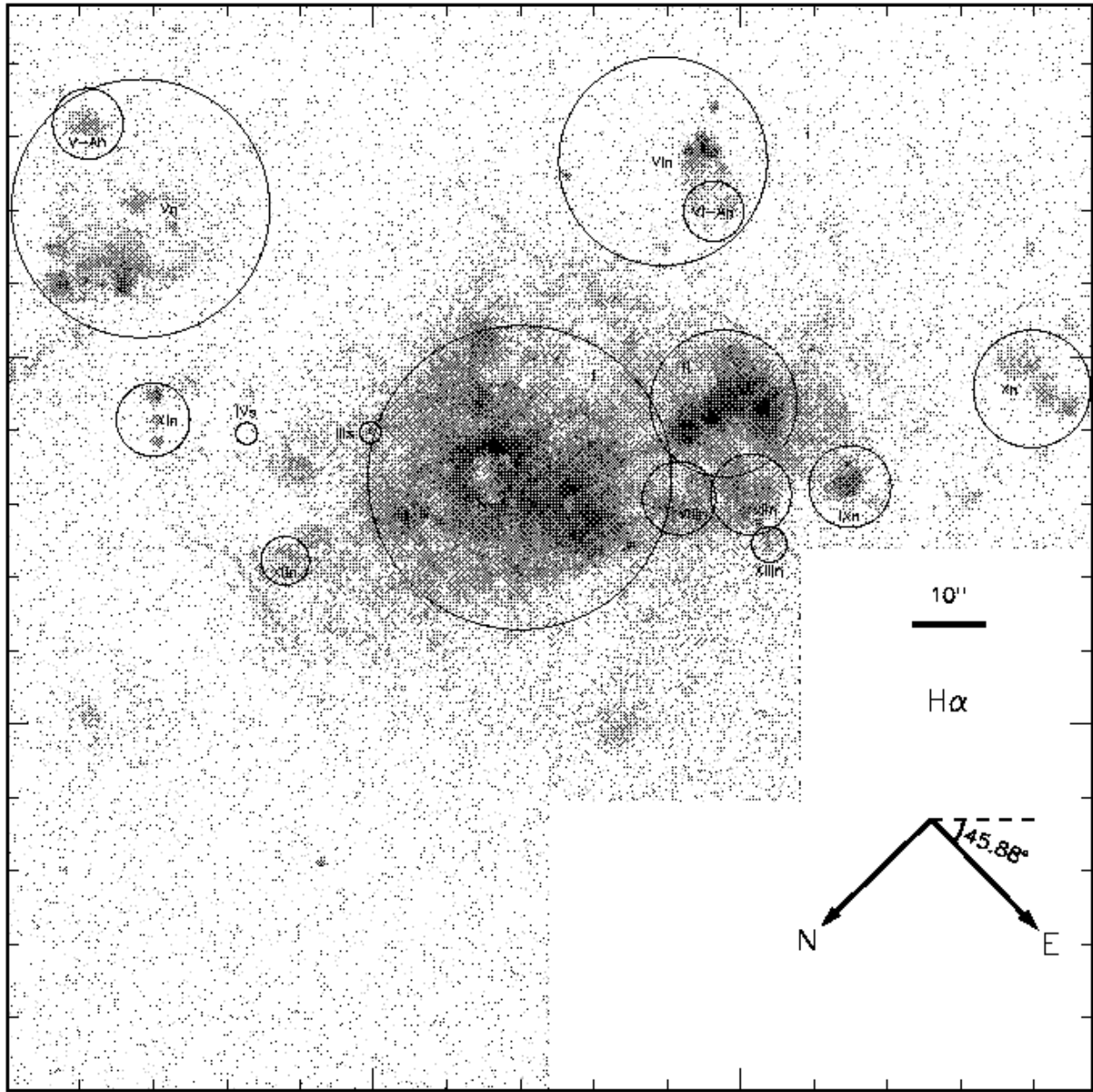


Fig. 2.— Logarithmic intensity scale, continuum subtracted H α WFPC2 image of NGC 4214. We show and label the unit nomenclature and corresponding circular apertures used in this work which do not correspond to subdivisions of the two main H II complexes, I and II. Those are shown in Fig. 7. Tick marks are shown for every hundredth pixel.

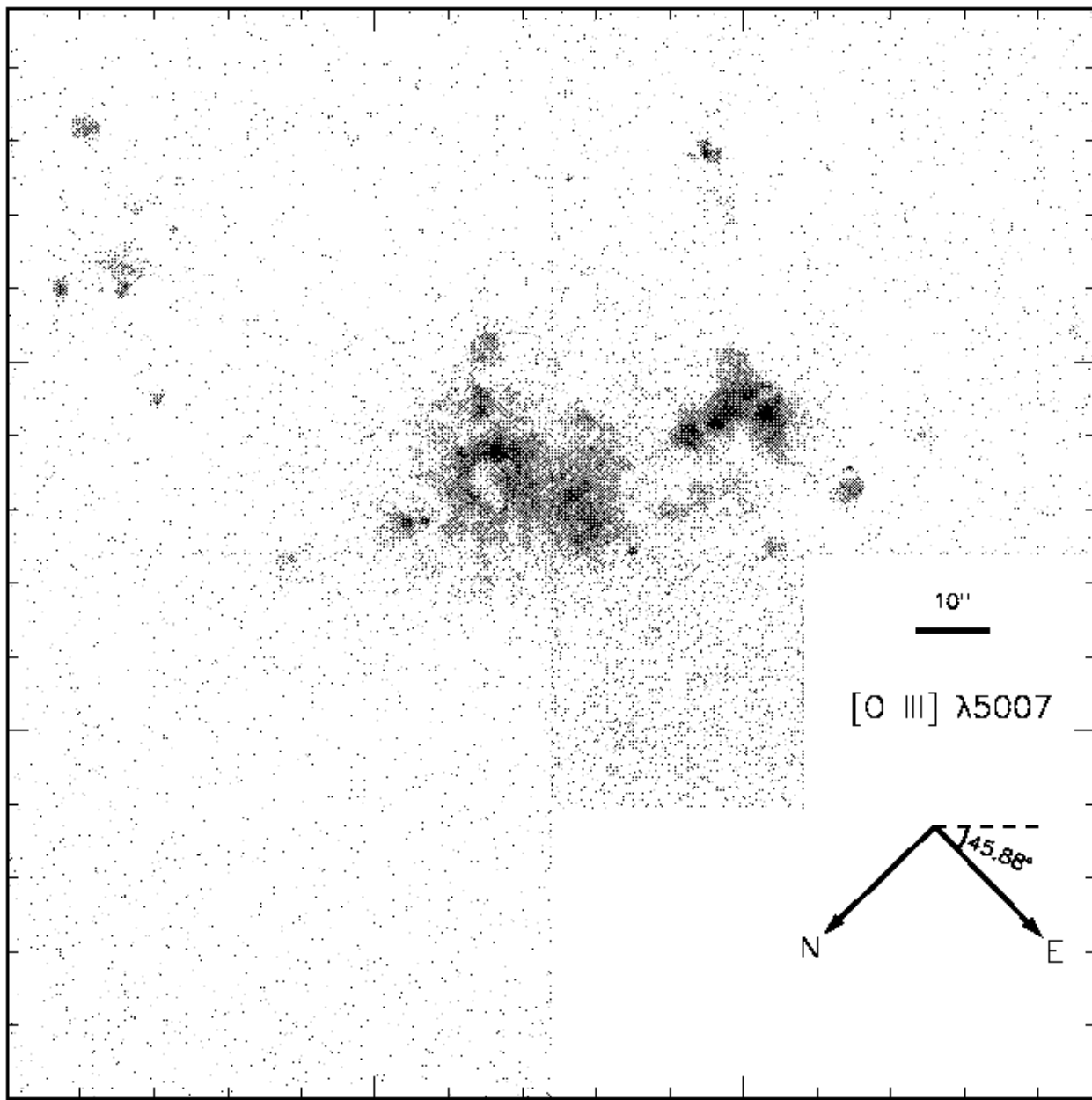


Fig. 3.— Logarithmic intensity scale, continuum subtracted $[\text{O III}] \lambda 5007$ WFPC2 image of NGC 4214. Tick marks are shown for every hundredth pixel.

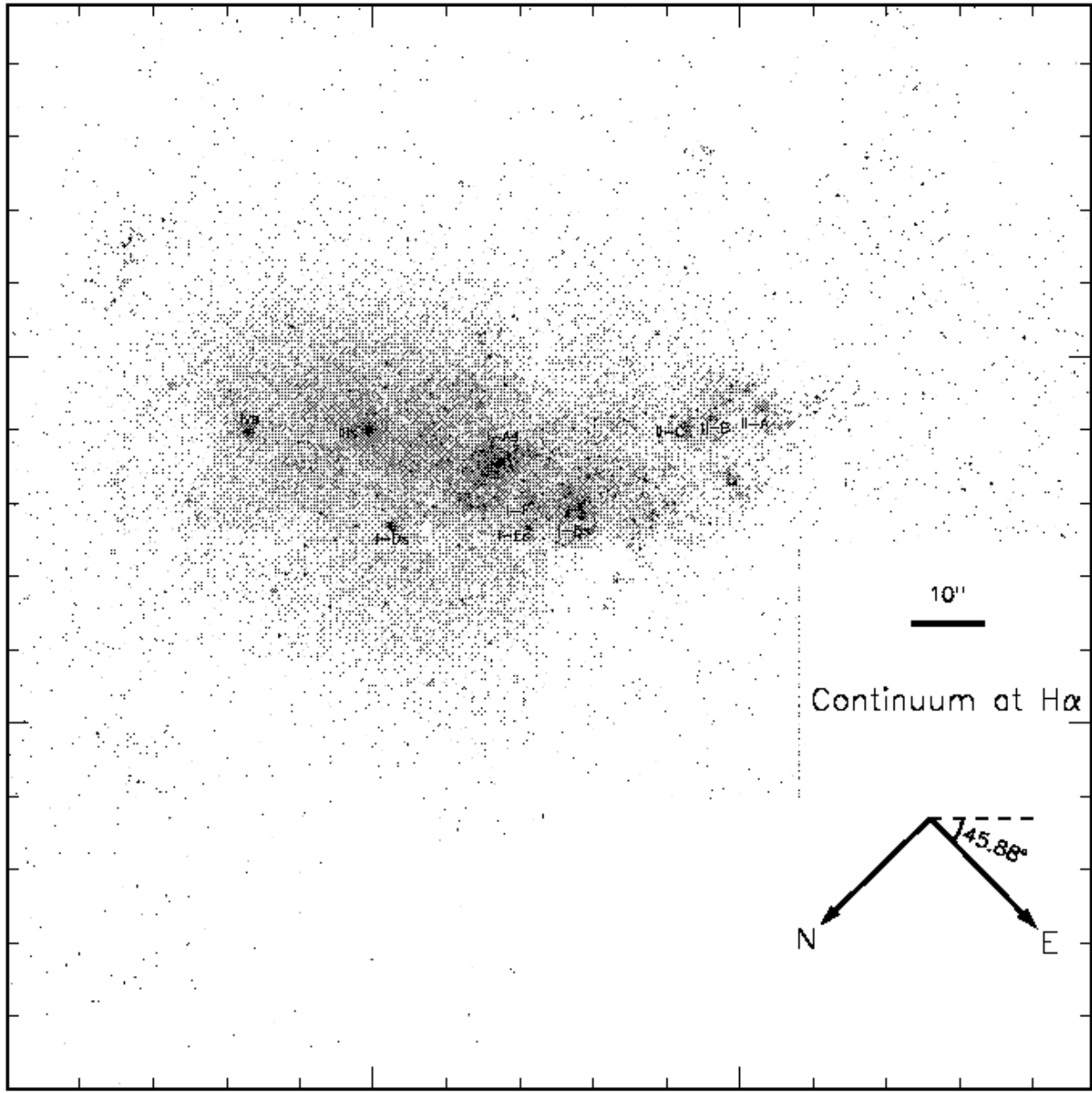


Fig. 4.— Logarithmic intensity scale H α continuum WFPC2 image of NGC 4214. This image is a linear combination of line emission subtracted V and R images. We label the units which correspond to the main continuum knots. Ticks marks are shown for every hundredth pixel.

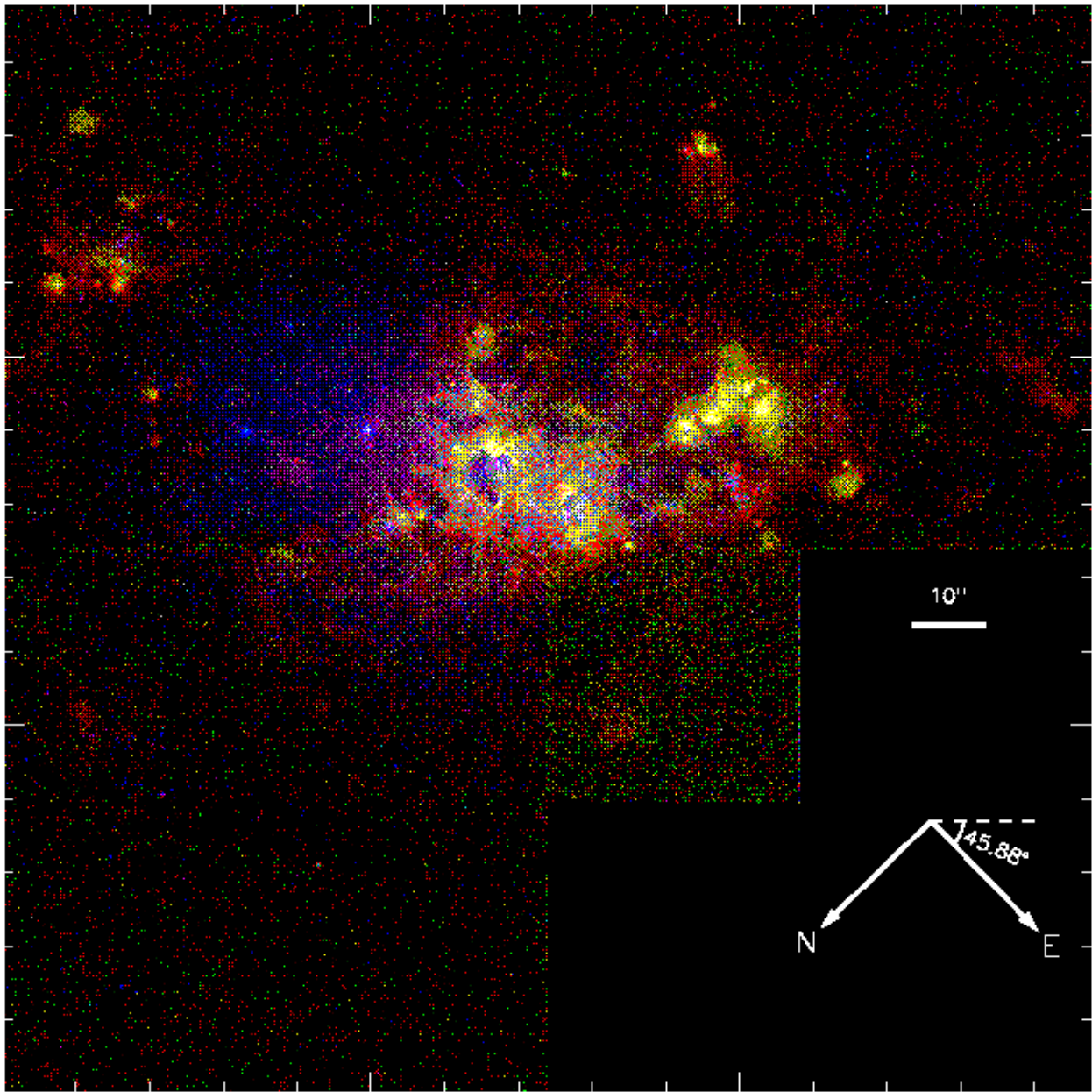


Fig. 5.— WFPC2 color mosaic of NGC 4214. Red corresponds to H α line emission, green to [O III] λ 5007 line emission, and blue to the continuum at H α . The intensity scale for each filter is logarithmic. The line emission filters have had the continuum contribution subtracted. Tick marks are shown for every hundredth pixel.

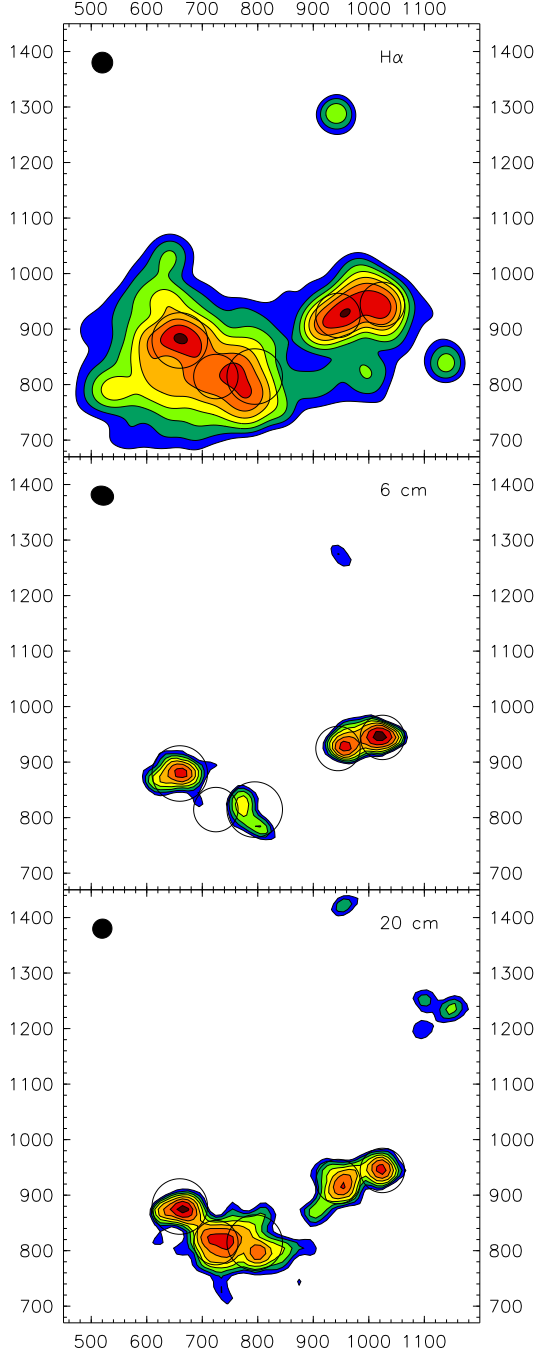


Fig. 6.— H α (top), 6 cm (middle), and 20 cm (bottom) contour plots of NGC 4214. The H α plot has been produced by degrading the resolution of the WFPC2 image to match approximately that of the other two, with the corresponding beam ellipsoids shown in the upper left corner in each case. The location of the five radio apertures is also shown. The eight levels are logarithmically spaced, with the minimum and maximum placed at $(15, 250) 10^{-16}$ erg s cm $^{-2}$ arcsec $^{-2}$ for H α , $(15, 75) 10^{-6}$ Jy arcsec $^{-2}$ for 6 cm, and $(22.5, 90) 10^{-6}$ Jy arcsec $^{-2}$ for 20 cm, respectively. The orientation is the same as in Fig. 2 and the coordinates are measured in pixels starting at the bottom left corner of the WFPC2 field.

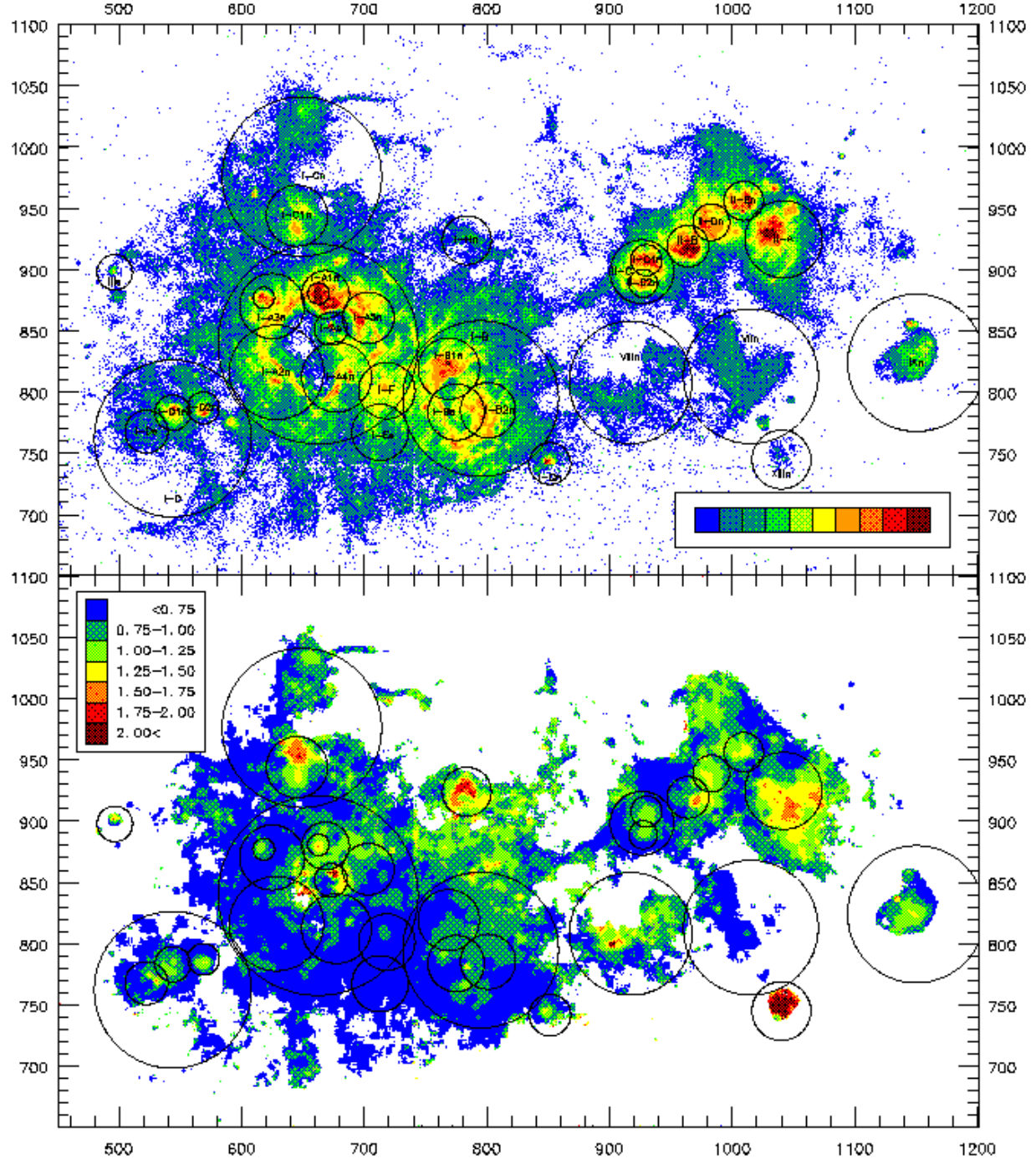


Fig. 7.— Top: Central area of the continuum subtracted H α WFPC2 image. The intensity scale is logarithmic between 20 and 1000 10^{-16} erg s $^{-1}$ cm $^{-2}$ arcsec $^{-2}$. The apertures in this area are shown, with the exception of I and II (see Fig. 2). All shown apertures are labelled, with the exception of the small I-A1n and I-A3n ones. The orientation is the same as in Fig. 2 and the coordinates are measured in pixels starting at the bottom left corner of the WFPC2 field. Bottom: [O III] $\lambda 5007$ / H α map of the same area as the top part. The intensities were smoothed with a 5 pixel box before evaluating the ratio and the areas left in white have H α or [O III] $\lambda 5007$ intensities less than 15 10^{-16} erg s $^{-1}$ cm $^{-2}$ arcsec $^{-2}$. The same apertures are shown again to guide the eye.

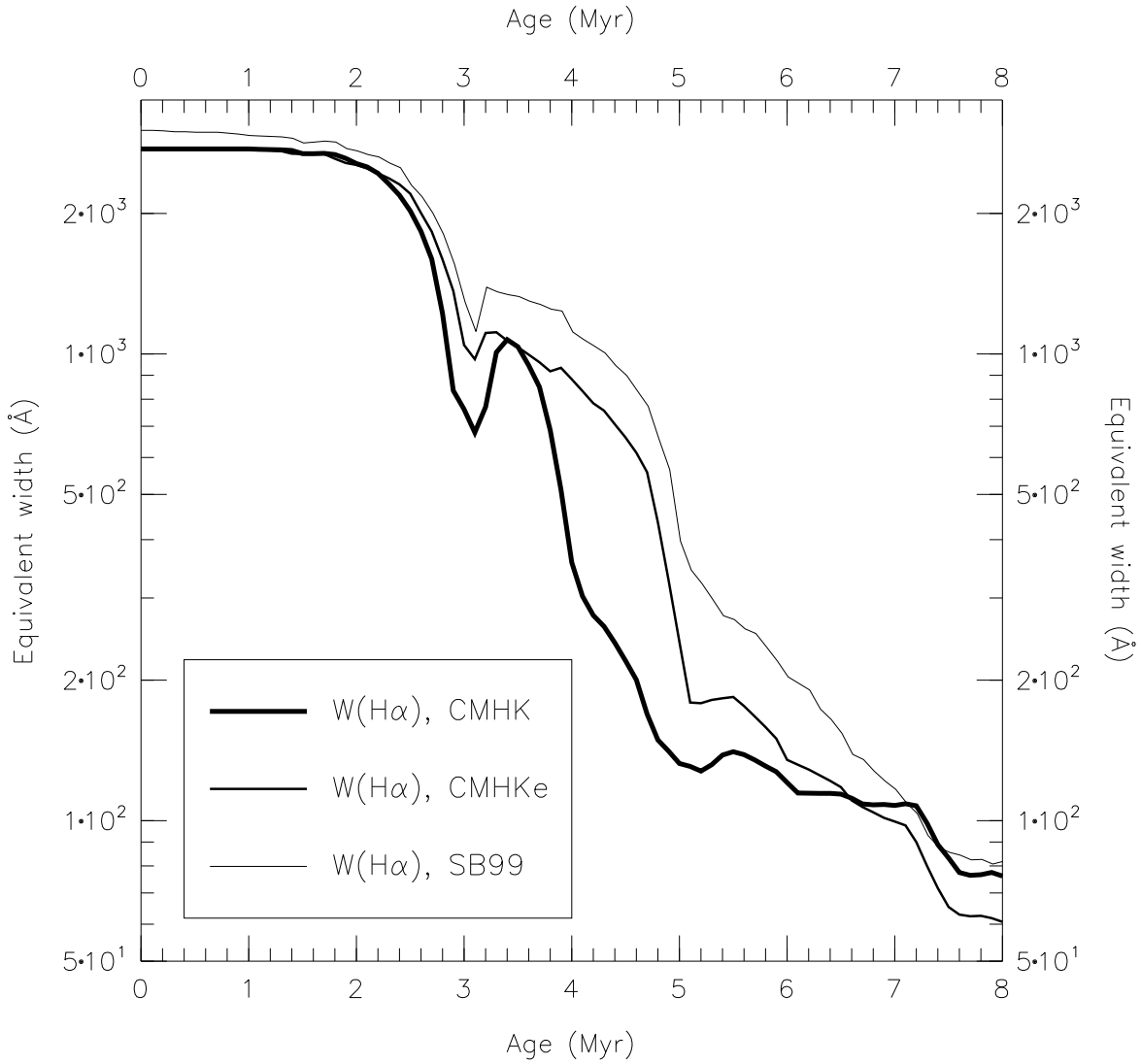


Fig. 8.— Predictions for $W(\text{H}\alpha)$ as a function of age from different evolutionary synthesis models. The first two plots are from the models of Cerviño et al. (2000) (CMHK, online version available at <http://www.laeff.esa.es/~mcs/model>) while the third one is from the Starburst 99 models of Leitherer et al. (1999) (SB99, online version available at <http://www.stsci.edu/science/starburst99>). The first CMHK model uses tracks with the standard mass-loss rate (Schaerer et al. 1993), while the other two models use tracks with an enhanced mass-loss rate for massive stars (Meynet et al. 1994). The atmospheric models used are Mihalas (1972) and Kurucz (1979) (CMHK standard mass-loss); Kurucz (1979), Schmutz et al. (1992), and Schaerer et al. (1996) (CMHK enhanced mass-loss); and Schmutz et al. (1992) and Lejeune et al. (1997) (SB99). The two CMHK models assume that 30% of the hydrogen ionizing photons are lost (absorbed by dust or escaped to the intergalactic medium) and use an upper mass limit of $120 M_{\odot}$. The SB99 models assume that no hydrogen ionizing photons are lost and use an upper mass limit of $100 M_{\odot}$. All cases are for $Z = 0.004$ and Salpeter IMF.

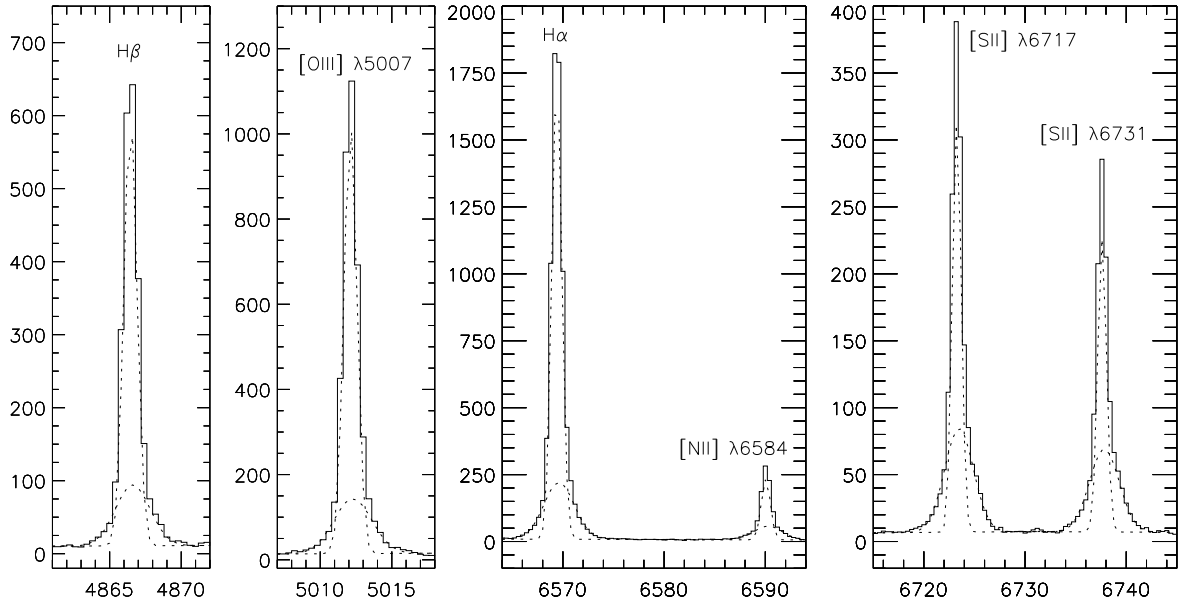


Fig. 9.— SNR optical spectrum extracted from the MMTM data. The fits for the narrow and wide components are shown. The units are Å and 10^{-17} erg s $^{-1}$ cm $^{-2}$ Å $^{-1}$ arcsec $^{-2}$ for the vertical and horizontal axes, respectively.

Table 1. Cycle 6 HST Observations of NGC 4214.

Filter	Band	Images	Exp. time (s)
F656N	H α	u3n8010fm + gm	800 + 800
F502N	[O III] λ 5007	u3n8010dm + em	700 + 800
F336W	WFPC2 U	u3n80101m + 2m + 3m	260 + 900 + 900
F555W	WFPC2 V	u3n80104m + 5m + 6m	100 + 600 + 600
F702W	WFPC2 wide R	u3n80107m + 8m	500 + 500
F814W	WFPC2 I	u3n8010am + bm + cm	100 + 600 + 600

Table 2. Unit nomenclature and corresponding circular apertures used in this work.

name	old name/description ^a	chip ^b	x^c (pix.)	y^c (pix.)	radius ($''$)	α (J2000) 12^h15^m+	δ (J2000) $36^\circ+$
I-A1n	knot 3 (small aperture)	3	662.50	880.50	0.87	39 ^h 214	19'33''75
I-A1n	knot 3 (interm. aperture)	3	668.25	879.75	1.94	39 ^h 250	19'33''39
I-A2n	knot 10	3	628.25	816.25	3.83	39 ^h 397	19'40''60
I-A3n	knot 8 (small aperture)	3	618.00	877.00	0.87	38 ^h 983	19'37''17
I-A3n	knot 8 (interm. aperture)	3	624.75	870.25	2.64	39 ^h 060	19'37''14
I-A4n	knot 9	3	677.25	812.25	2.84	39 ^h 697	19'37''38
I-A5n	knot 7	3	703.25	860.75	2.09	39 ^h 558	19'32''20
I-As	knot A (small aperture)	3	672.75	851.75	1.34	39 ^h 441	19'34''99
I-A	knot A (large aperture)	3	662.25	839.25	8.12	39 ^h 456	19'36''59
I-B1n	knot 5	2	768.75	819.25	2.49	40 ^h 157	19'30''18
I-B2n	knot 6	2	800.75	785.25	2.24	40 ^h 539	19'30''25
I-Bs	knot B (small aperture)	2	774.75	783.75	2.29	40 ^h 400	19'32''18
I-B	knot B (large aperture)	2	794.75	794.75	6.32	40 ^h 449	19'30''03
I-C1n	knot W of knot 3*	3	645.00	944.00	2.49	38 ^h 741	19'30''63
I-Cn	W region of NW complex*	3	649.00	976.00	6.47	38 ^h 577	19'28''15
I-D1n	knot 12 (N)	3	543.75	783.25	1.44	39 ^h 115	19'48''91
I-D2n	knot 12 (S)	3	568.75	787.25	1.29	39 ^h 232	19'46''85
I-Ds	knot C	3	522.25	767.75	1.74	39 ^h 086	19'51''51
I-D	knot C-12	3	543.75	762.25	6.37	39 ^h 240	19'50''34
I-Es	knot F	3	712.75	767.25	2.29	40 ^h 155	19'37''93
I-F	knot I	3	718.25	801.25	2.29	39 ^h 990	19'35''21
I-Gn	knot 11	2	851.25	741.75	1.69	41 ^h 083	19'29''66
I-Hn	froth	2	783.50	924.00	1.99	39 ^h 624	19'21''98
I	NW complex	3	700.00	836.00	20.62	39 ^h 686	19'34''12
II-A	knot 2-K	2	1041.75	924.75	3.14	41 ^h 097	19'03''60
II-B	knot 1-D	2	963.75	919.25	1.69	40 ^h 683	19'09''54
II-C1n	knot 4-E (S)	2	930.00	907.75	1.27	40 ^h 557	19'12''73
II-C2n	knot 4-E (N)	2	927.25	888.75	1.15	40 ^h 654	19'14''23
II-C	knot 4-E	2	926.25	898.25	2.59	40 ^h 592	19'13''65
II-Dn	knot L (N)	2	982.75	938.75	1.49	40 ^h 676	19'06''84
II-En	knot L (S)	2	1009.25	956.25	1.59	40 ^h 725	19'03''74
II	SE complex	2	977.75	937.25	9.96	40 ^h 657	19'07''30
IIIs	nucleus*	3	496.50	897.75	1.44	38 ^h 174	19'44''44
IVs	old cluster?*	3	327.50	896.25	1.47	37 ^h 222	19'56''66
V-An	Far W region (high exc. zone)*	3	111.00	1318.00	4.78	33 ^h 494	19'43''10
Vn	Far W region*	3	183.00	1203.00	17.53	34 ^h 578	19'45''88
VI-An	Far S region (high exc. zone)*	2	964.00	1199.00	4.08	39 ^h 031	18'50''14
VIn	Far S region*	2	895.00	1267.00	14.14	38 ^h 236	18'50''35
VIIIn	knot 15	2	1015.00	813.00	5.48	41 ^h 602	19'13''20
VIIIIn	knot 14	2	917.00	808.00	4.98	41 ^h 070	19'20''50
IXn	knot 13	2	1150.00	824.00	5.58	42 ^h 309	19'02''83
Xn	old shell*	2	1398.00	957.00	7.97	42 ^h 938	18'35''98
XIn	knot E of old cluster*	3	200.00	915.00	4.98	36 ^h 383	20'04''47
XIIIn	high exc. region N of knot 12	4	380.00	723.00	3.29	38 ^h 540	20'04''62
XIIIIn	high exc. region E of knot 15*	2	1040.00	745.00	2.39	42 ^h 143	19'16''09

^aSee Maíz-Apellániz et al. (1998) or Maíz-Apellániz (1999).

^bWFPC2 chip at the aperture center.

^cCoordinates of the aperture center in our mosaics.

*Extinction uncertain.

Table 3. Integrated H α , [O III] λ 5007, and H α continuum fluxes obtained from different extinction models for the apertures in Table 2.

name	log $F(\text{H}\alpha)$ (ergs s^{-1} cm^{-2})						log $F(\text{[O III]} \lambda 5007)$ (ergs s^{-1} cm^{-2})						log $F(\lambda 6563)$ (ergs s^{-1} cm^{-2} \AA^{-1})		
	no ext. ^a	ext. 1 ^b	ext. 2 ^c	% 1 ^d	% 2 ^e	no ext. ^a	ext. 1 ^b	ext. 2 ^c	% 1 ^d	% 2 ^e	no ext. ^a	ext. 1 ^b	% 1 ^d		
I-A1n	-12.68	-12.42	-12.29	84	151	-12.60	-12.23	-12.05	137	254	-15.82	-15.55	86		
I-A1n	-12.30	-12.11	-12.02	54	92	-12.27	-11.99	-11.86	90	159	-15.20	-15.05	42		
I-A2n	-12.40	-12.26	-12.22	37	48	-12.56	-12.37	-12.32	54	73	-14.71	-14.55	44		
I-A3n	-13.17	-12.86	-12.72	103	183	-13.20	-12.77	-12.59	165	302	-16.13	-15.81	106		
I-A3n	-12.47	-12.25	-12.15	67	110	-12.58	-12.27	-12.13	106	182	-15.05	-14.86	56		
I-A4n	-12.54	-12.35	-12.24	53	100	-12.68	-12.43	-12.29	78	148	-15.06	-14.87	54		
I-A5n	-12.56	-12.46	-12.44	28	32	-12.62	-12.47	-12.45	38	47	-15.13	-15.01	32		
I-As	-13.22	-13.17	-13.16	12	13	-13.22	-13.15	-13.14	17	20	-14.84	-14.80	10		
I-A	-11.58	-11.40	-11.32	50	79	-11.68	-11.43	-11.32	77	130	-14.05	-13.89	43		
I-B1n	-12.39	-12.28	-12.27	27	32	-12.51	-12.37	-12.34	39	49	-15.12	-15.02	24		
I-B2n	-12.52	-12.34	-12.29	52	69	-12.62	-12.38	-12.31	75	104	-15.14	-14.99	41		
I-Bs	-12.53	-12.41	-12.39	31	37	-12.63	-12.46	-12.42	47	59	-14.98	-14.86	30		
I-B	-11.81	-11.68	-11.61	37	61	-11.95	-11.76	-11.68	52	85	-14.39	-14.27	33		
I-C1n	-12.79	-12.74	-12.73	12	13	-12.74	-12.67	-12.66	17	19	-15.26	-15.21	12		
I-Cn	-12.29	-12.23	-12.21	14	21	-12.37	-12.28	-12.25	21	30	-14.54	-14.48	15		
I-D1n	-13.11	-13.00	-12.93	30	53	-13.14	-12.99	-12.92	41	67	-15.79	-15.65	37		
I-D2n	-13.27	-13.12	-12.91	41	128	-13.32	-13.12	-12.89	61	169	-15.90	-15.72	49		
I-Ds	-13.45	-13.30	-13.28	39	49	-13.56	-13.38	-13.33	53	69	-15.38	-15.29	25		
I-D	-12.37	-12.22	-12.13	41	74	-12.53	-12.33	-12.21	59	107	-14.56	-14.40	43		
I-Es	-12.87	-12.72	-12.69	41	51	-13.20	-12.99	-12.94	61	80	-15.29	-15.11	49		
I-F	-12.56	-12.43	-12.41	35	41	-12.81	-12.63	-12.59	51	64	-15.20	-15.07	36		
I-Gn	-13.32	-12.95	-11.90	132	2543	-13.36	-12.86	-11.72	214	4177	-15.85	-15.50	123		
I-Hn	-13.43	-13.31	-13.29	31	36	-13.30	-13.14	-13.10	46	58	-15.67	-15.56	29		
I	-11.17	-11.02	-10.89	40	88	-11.29	-11.09	-10.90	60	144	-13.48	-13.36	33		
II-A	-12.23	-11.97	-11.71	83	232	-12.17	-11.82	-11.52	124	349	-15.19	-14.93	83		
II-B	-12.39	-12.26	-12.10	32	93	-12.35	-12.16	-11.89	53	186	-15.52	-15.40	33		
II-C1n	-12.75	-12.72	-12.72	8	9	-12.76	-12.72	-12.71	10	12	-15.69	-15.66	7		
II-C2n	-13.03	-13.01	-13.01	4	4	-13.06	-13.04	-13.03	5	5	-15.91	-15.89	3		
II-C	-12.41	-12.35	-12.33	14	20	-12.46	-12.39	-12.36	18	26	-15.26	-15.19	18		
II-Dn	-12.68	-12.55	-12.53	34	41	-12.63	-12.45	-12.42	49	61	-15.75	-15.62	36		
II-En	-12.69	-12.55	-12.53	37	44	-12.66	-12.47	-12.44	54	67	-15.74	-15.60	39		
II	-11.59	-11.43	-11.24	43	121	-11.59	-11.36	-11.09	69	216	-14.28	-14.15	37		
IIIs	-13.85	-13.80	-13.80	12	13	-13.99	-13.92	-13.91	16	19	-15.05	-15.00	12		
IVs	-15.28	-15.23	-15.22	12	13	-14.59	-14.52	-14.51	17	19	-15.30	-15.25	12		
V-An	-13.41	-13.36	-13.36	12	13	-13.23	-13.16	-13.15	17	19	-15.90	-15.85	12		
Vn	-12.25	-12.20	-12.19	12	13	-12.47	-12.40	-12.39	17	19	-14.24	-14.19	12		
VI-An	-13.46	-13.41	-13.40	12	13	-13.35	-13.28	-13.27	17	19	-15.58	-15.53	12		
VIIn	-12.53	-12.48	-12.48	12	13	-12.57	-12.50	-12.49	17	19	-14.54	-14.49	12		
VIIIn	-12.65	-12.52	-12.40	35	80	-12.95	-12.77	-12.63	51	112	-14.87	-14.75	33		
VIIIIn	-12.73	-12.65	-12.63	19	24	-12.80	-12.70	-12.67	27	35	-14.83	-14.74	22		
IXn	-12.78	-12.59	-12.31	55	196	-12.87	-12.60	-12.25	83	309	-15.20	-14.99	62		
Xn	-13.03	-12.98	-12.98	12	13	-13.34	-13.27	-13.26	17	19	-15.09	-15.04	12		
XIn	-13.40	-13.35	-13.35	12	13	-13.72	-13.65	-13.64	16	19	-15.06	-15.00	12		
XIIIn	-13.45	-13.39	-13.39	13	14	-13.46	-13.37	-13.36	20	25	-15.32	-15.27	12		
XIIIIn	-13.67	-13.44	-13.24	72	173	-13.48	-13.12	-12.87	127	309	-15.99	-15.75	71		
All	-10.86	-10.74	-10.62	33	76	-10.96	-10.78	-10.59	52	133	-12.90	-12.82	20		

^aNo extinction correction applied.^bForeground screen correction applied.^cGas/dust mixed correction applied.^dPercentage increase between first and second columns.^ePercentage increase between first and third columns.

Table 4. Integrated [O III] $\lambda 5007/\text{H}\alpha$ and $W(\text{H}\alpha)$ obtained from different extinction models for the apertures in Table 2.

name	[O III] $\lambda 5007/\text{H}\alpha$						$W(\text{H}\alpha)$ (Å)							
	no ext. ^a	ext. 1 ^b	ext. 2 ^c	% 1 ^d	% 2 ^e	no ext. ^a	line ext. 1 ^b	line ext. 2 ^c	all ext. ^f	% line ext. 1 ^d	% line ext. 2 ^e	% all ext. ^g		
I-A1n	1.21	1.56	1.71	28	41	1368	2521	3433	1348	84	151	-1		
I-A1n	1.07	1.32	1.45	22	34	791	1222	1519	858	54	92	8		
I-A2n	0.68	0.76	0.80	12	17	206	283	305	196	37	48	-4		
I-A3n	0.95	1.23	1.34	30	41	900	1831	2554	888	103	183	-1		
I-A3n	0.77	0.94	1.03	23	34	381	638	801	408	67	110	7		
I-A4n	0.72	0.84	0.89	16	24	328	504	656	327	53	100	0		
I-A5n	0.88	0.96	0.98	8	11	372	477	493	360	28	32	-3		
I-As	0.99	1.03	1.05	4	6	42	48	48	43	12	13	1		
I-A	0.80	0.94	1.02	18	27	294	442	529	308	50	79	4		
I-B1n	0.75	0.82	0.84	9	12	535	683	707	551	27	32	2		
I-B2n	0.79	0.91	0.95	15	20	422	642	716	454	52	69	7		
I-Bs	0.80	0.89	0.92	11	15	282	371	388	286	31	37	1		
I-B	0.74	0.82	0.84	11	14	378	519	611	389	37	61	3		
I-C1n	1.12	1.17	1.18	4	5	300	336	339	299	12	13	0		
I-Cn	0.84	0.89	0.91	5	7	176	202	212	175	14	21	0		
I-D1n	0.93	1.02	1.02	8	9	477	620	730	451	30	53	-5		
I-D2n	0.89	1.01	1.05	13	18	424	601	967	402	41	128	-5		
I-Ds	0.77	0.85	0.88	10	13	86	120	128	96	39	49	11		
I-D	0.69	0.78	0.83	12	18	154	219	270	153	41	74	0		
I-Es	0.47	0.53	0.56	14	19	261	369	394	247	41	51	-5		
I-F	0.56	0.63	0.65	12	16	440	595	622	434	35	41	-1		
I-Gn	0.92	1.25	1.49	35	61	340	791	8999	353	132	2543	3		
I-Hn	1.33	1.49	1.54	12	16	175	229	238	176	31	36	1		
I	0.76	0.87	0.98	14	29	206	289	388	216	40	88	5		
II-A	1.16	1.41	1.57	21	35	902	1660	2999	907	83	232	0		
II-B	1.08	1.26	1.60	16	48	1368	1807	2647	1353	32	93	-1		
II-C1n	0.99	1.01	1.02	1	2	871	943	953	876	8	9	0		
II-C2n	0.93	0.94	0.94	0	1	753	786	789	756	4	4	0		
II-C	0.88	0.91	0.93	3	5	713	818	857	690	14	20	-3		
II-Dn	1.14	1.26	1.30	10	14	1179	1589	1664	1164	34	41	-1		
II-En	1.07	1.20	1.24	12	16	1117	1541	1613	1108	37	44	0		
II	0.98	1.16	1.41	17	43	498	715	1100	521	43	121	4		
III	0.73	0.76	0.77	3	5	16	18	18	16	12	13	0		
IV	4.88	5.09	5.15	4	5	1	1	1	1	12	13	0		
V-An	1.53	1.59	1.61	4	5	304	341	344	304	12	13	0		
Vn	0.60	0.62	0.63	4	5	99	111	112	99	12	13	0		
VI-An	1.28	1.34	1.36	4	5	133	149	150	133	12	13	0		
VIn	0.91	0.95	0.96	4	5	103	116	117	103	12	13	0		
VIIIn	0.50	0.56	0.59	11	17	166	226	299	169	35	80	1		
VIIIIn	0.84	0.89	0.91	6	8	127	151	158	124	19	24	-2		
IXn	0.82	0.97	1.13	18	38	265	411	785	252	55	196	-4		
Xn	0.49	0.51	0.52	4	5	116	130	131	116	12	13	0		
XIn	0.48	0.50	0.51	4	5	45	51	51	45	12	13	0		
XIIIn	0.98	1.04	1.07	7	9	75	84	86	75	13	14	0		
XIIIIn	1.55	2.05	2.33	31	49	205	355	562	206	72	173	0		
All	0.80	0.91	1.06	13	32	110	148	194	122	33	76	11		

^aNo extinction correction applied.

^bForeground screen correction applied to line emission.

^cMixed gas/dust correction applied to line emission.

^dPercentage increase between first and second columns.

^ePercentage increase between first and third columns.

^fForeground screen correction applied to both line emission and continuum.

^gPercentage increase between first and fourth columns.

Table 5. Radio aperture data.

name	α (J2000) 12 ^h 15 ^m +	δ (J2000) 36°+	radius (arcsec)	$\log F^a$ (6 cm)	$\log F^a$ (20 cm)	$\log F^b$ (H α)	$\log F^c$ (H α)	α^d	τ_{rad}^e	τ_{Bal}^f
I-A	39 ^h 165	19'33"97	5.00	-2.64	-2.48	-11.91	-11.73	-0.31	1.10 - 1.39	0.41
I-F	39 ^h 926	19'34"03	4.00	-3.22	-2.51	-12.12	-11.99	-1.36	—	0.31
I-B	40 ^h 338	19'29"11	5.00	-2.85	-2.43	-12.05	-11.91	-0.81	—	0.30
II-AE	40 ^h 937	19'03"70	4.00	-2.70	-2.68	-12.12	-11.89	-0.04	0.86	0.53
II-BCD	40 ^h 582	19'10"74	4.00	-2.84	-2.62	-12.08	-11.96	-0.42	1.19 - 1.52	0.27

^alog(radio flux) in Jy.

^bMeasured log(H α flux) in erg s $^{-1}$ cm $^{-2}$.

^cExtinction-corrected log(H α flux) in erg s $^{-1}$ cm $^{-2}$ using the Balmer ratio and a foreground screen model.

^dRadio spectral index.

^eOptical depth at H α measured from the radio / H α ratio.

^fOptical depth at H α measured from the Balmer ratio.

Table 6. Excitation ratios at the SNR location.

ratio	narrow comp.	wide comp.
[N II] $\lambda 6584$ / H α	0.13 ± 0.01	0.24 ± 0.05
[S II] $\lambda 6717 + \lambda 6731$ / H α	0.31 ± 0.01	0.66 ± 0.09
[O III] $\lambda 5007$ / H α	1.71 ± 0.08	1.55 ± 0.35

Table 7. Integrated quantities as a function of pixel flux.

log (pixel flux) ^a	log (% <i>N</i>) ^b	% H α ^c	% [O III] $\lambda 5007^c$	exc. ratio ^d
-17.0 or less	1.96	26.3	20.2	0.62
-17.0 to -16.5	0.77	16.1	16.8	0.83
-16.5 to -16.0	0.43	21.8	21.4	0.79
-16.0 to -15.5	-0.02	22.1	23.1	0.84
-15.5 to -15.0	-0.79	10.2	13.3	1.04
-15.0 to -14.5	-1.76	2.9	4.5	1.27
-14.5 or more	-3.02	0.5	1.1	1.69

^aThe flux for a single pixel is measured as the mean of H α and [O III] $\lambda 5007$ after a 3×3 pixel box smoothing filter is applied to low intensity areas. The units are erg s $^{-1}$ cm $^{-2}$.

^bPercentage of pixels in that flux bin.

^cPercentage of the total flux in that bin.

^dExcitation ratio [O III] $\lambda 5007$ / H α for that flux bin.